Material Science and Technology Division

Heavy Vehicle Propulsion Materials Program
Quarterly Progress Report for
October through December 2006

D. R. Johnson
Technical Project Manager

Prepared for
U.S. Department of Energy
Assistant Secretary for Energy Efficiency and Renewable Energy
Office of FreedomCAR and Vehicle Technologies Program
VT 05 01 020

Prepared by the
OAK RIDGE NATIONAL LABORATORY
Oak Ridge, Tennessee 37831-6066
Managed by
UT-Battelle, LLC
for the Department of Energy
Under contract DE-AC05-00OR22725

CONTENTS

Materials for Fuel Efficient Emission Reduction

Catalyst Characterization, CRADA with Cummins (ORNL) – no report this period

Characterization of Catalyst Microstructures and Deactivation Mechanisms (ORNL)

Catalysis by First Principles - Can Theoretical Modeling and Experiments Play a Complimentary Role in Catalysis? (ORNL)

Durability of Particulate Filters, CRADA with Cummins (ORNL) – no report this period

Materials for Advanced Combustion

Mechanical Reliability of PZT Piezo-Stack Actuators for Fuel Injectors **(ORNL)**

Advanced Cast Austenitic Stainless Steels for High Temperature Components, CRADA with Caterpillar (ORNL)

Friction and Wear Reduction in Diesel Engine Valve Trains (ORNL)

*Lightweight Valve Train Materials (*Caterpillar)

NDE of Diesel Engine Components (Argonne)

Life Prediction of Diesel Engine Components (ORNL)

Modeling of Thermoelectrics **(ORNL)**

Powder Processing of Nanostructured Alloys Produced by Machining (Purdue)

Ultra-High Resolution Electron Microscopy for Characterization of Catalyst Microstructures and De-activation Mechanisms

L. F. Allard, D. A. Blom, C. K. Narula, M. A. O'Keefe, M. J. Yacaman and S. A. Bradley
Oak Ridge National Laboratory

Objective/Scope

The objective of the research is to characterize the microstructures of catalyst materials of interest for the treatment of NO_x emissions in diesel and lean-burn gasoline engine exhaust systems. The research heavily utilizes new capabilities and techniques for ultra-high resolution transmission electron microscopy with the HTML's aberration-corrected electron microscope. The research is focused on understanding the effects of reaction conditions on the changes in morphology of heavy metal species on "real" catalyst support materials (typically oxides), and the understanding of the structures of model mono-, bi- and multi-metallic catalyst systems of known particle composition. With the former systems, these changes are being studied utilizing samples treated in both steady-state bench reactors and a special *ex-situ* catalyst reactor system especially constructed to allow appropriate control of the reaction. Model samples of nanoparticulates of controlled composition on carbon or oxide supports are also being studied in collaboration with the catalysis group at the University of Texas-Austin (Prof. M. Jose-Yacaman and students). Studies of the behavior of Pt species on oxide substrates are also being conducted with colleague S. A. Bradley of UOP Co.

Technical Progress

Bimetallic clusters and nanoparticles attract great interest due to their unique catalytic, electronic, and optical properties that differ from those of the corresponding monometallic components [1-5]. For instance, it is well known that adding a second metallic component enhances the activity, selectivity and stability of a pure metal catalyst. This behavior may originate from an ensemble or a ligand effect. The properties of bimetallic nanoparticles can vary dramatically not only with size, as happens in pure nanoclusters, but also with chemical composition. Controlling their structure and chemical ordering can be the starting point to prepare the building blocks for specifically tailored cluster-assembled materials.

It has been reported in many cases that bimetallic systems display a core/shell structure, where a thin shell of metal B surrounds a core of metal A. The B overlayer is usually strained, and thus can present prominent catalytic properties. The chemical and physical properties of bimetallic nanoparticles exhibiting core/shell structure strongly depend on whether the two monometallic elements are chemically segregated or intimately alloyed. These materials can be grown by different microscopic mechanisms, either involving shell-by-shell growth on pre-existing smaller clusters, or by a structural transformation of the clusters. Our approach consists of synthesizing polymer-protected Au-Pd nanoparticles by means of the polyol method [6]. A core/shell structure was obtained in the colloids by the successive reduction of their corresponding metallic salts. Figure 1a is a high-angle annular dark-field (HA-ADF) STEM image of typical particles, recorded using the sub-Ångström probe in a JEOL 2200FS STEM/TEM equipped with a CEOS Co. aberration corrector. These particles show three regions of contrast comprising a dark central core (often faceted), a bright inner shell, and a distinct outer shell. The central core is only faintly evident in the simultaneously acquired bright-field image (Fig. 1b). The dark

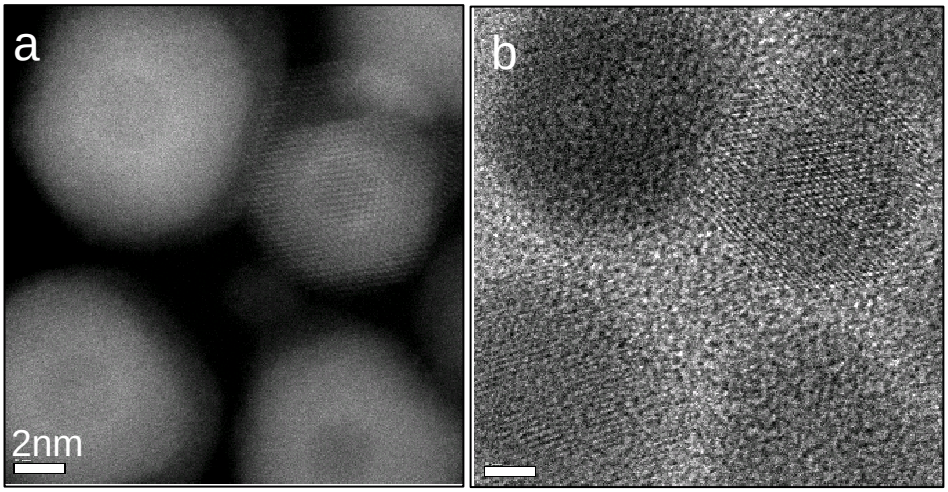

Fig. 1 a) HA-ADF image of typical Au1-Pd1 particles, showing dark core feature, with surrounding bright shell, and outer shell in darker contrast; b) corresponding BF image, simultaneously acquired. Core feature must be low atomic number (i.e. highly Pd rich), or a void, to give dark contrast in ADF image.

contrast of the core suggests the possibility of a void, as the reduced amount of material would result in lower scattering at high angles, and therefore lower contrast.

Electron holography results from our Hitachi HF-2000 FE-TEM, however, did not support this hypothesis, as there was no indication of a reduction in the phase profile consistent with the presence of a void in any of 10 particles imaged [7]. Figure 2a shows a phase image reconstructed from an electron hologram of one of ten different Au-Pd particles studied with this technique. The phase profile across the indicated line does not show a “dip” in phase intensity, as would be expected if the particle contained a central void that would be consistent with the dark central feature such as observed in the dark-field STEM image shown in Fig. 1. This feature was observed to be present in virtually every particle we imaged, in the size range from 5-10nm. Thus the dark contrast must be due to a significantly lower atomic number volume, and this can only be accounted for by presuming the core to be highly enriched in Pd. The first shell, in like fashion, must be enriched in Au (in this nominal 1:1 specimen), and the outer shell is likely to be higher in Pd. Preliminary EDS spectra confirmed higher Au in the bright contrast region, consistent with the image contrast observed. HA-ADF images of particles taken near zone-axis orientations consistently showed atomic column contrast through the entire particle, as seen in Fig. 3. Because of the similarity in the structure of Au and Pd, (FCC, 4.8% lattice mismatch) this suggests that the core formed as a facetted single crystal of Pd, and a first shell enriched in Au then grew epitactically on the core particle, transitioning finally into an outer shell enriched in Pd. This data provides information for computed models, to further correlate the observed image contrast to structure, chemistry and morphology.

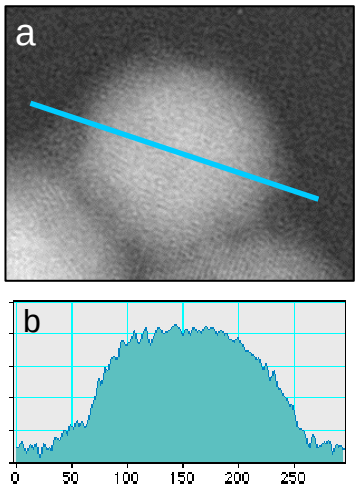

Fig. 2. a) Reconstructed phase image from hologram of a typical particle; b) phase profile showing no significant 'dip' in phase, suggesting the dark core feature is not a void.

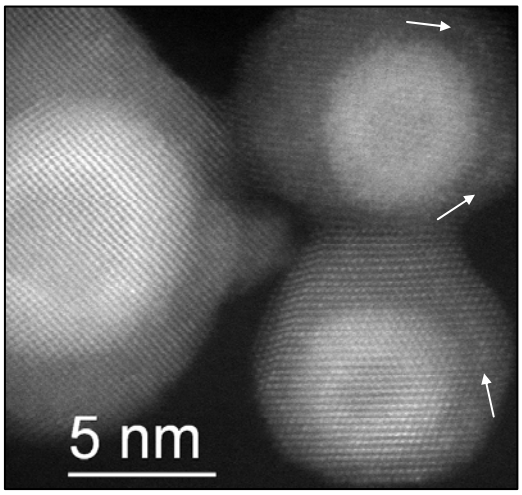

Fig. 3. Au-Pd3 particles, showing similar core feature, with thick outer shell. Note regions of bright contrast in outer shell that suggest Au enrichment (arrows).

References

[1] N. Toshima and T. Yonezawa, *New J. Chem*. (1998) 1179.
[2] T. Fujikawa, et al., *Appl. Catal. A* (2000), 192, 253.
[3] M. Jacquin, et al., *J. Catal.* (2004), 228, 447
[4] B. Pawelec, et al., *Appl. Catal. A* (2002), 223-225.
[5] S. C. Kim, *Catal. Today* (2003), 87, 51.
[6] D. García-Gutiérrez, C. Gutiérrez-Wing, L. Giovanetti, J. Ramallo-López, F. Requejo, M. José-Yacamán; *J. Phys. Chem. B* (2005) 109, 3813.
[7] L. F. Allard, E. Voelkl, D.S. Kalakkad, A. Datye, *J. Mat. Sci*., 29(21) (1994) 5612-14

Status of Milestones

On schedule

Communications/Visits/Travel

None this period

Publications

1. "On the Structure of Au/Pd Bimetallic Nanoparticles", S.J. Mejia-Rosales, C. Fernandes-Navarro, E. Perez-Tijerina, D. A. Blom, L. F. Allard and M. Jose-Yacaman, J. Physical Chemistry C, V.111(2007) PP. 1256-1260.

2. "Observation of Pt Atoms, Clusters and Rafts on Oxide Supports, by Sub-Ångström Z-Contrast Imaging in an Aberration-Corrected STEM/TEM,"
D. A. Blom, S. A. Bradley, W. Sinkler and L. F. Allard, *Microscopy and Microanalysis (Supp 2) 2006*, Cambridge University Press, p. 50.

3. "Early Results from an Aberration-Corrected JEOL 2200FS STEM/TEM at Oak Ridge National Laboratory," D. A. Blom, L. F. Allard, S. Mishina, and M. A. O'Keefe, Microsc. and Microanal. in press, 2006.

Catalysis by First Principles - Can Theoretical Modeling and Experiments Play a Complimentary Role in Catalysis?

C. Narula, W. Shelton, M. Moses, L. Allard
Oak Ridge National Laboratory

Objective/Scope

This research focuses on an integrated approach between computational modeling and experimental development, design and testing of new catalyst materials, that we believe will rapidly identify the key physiochemical parameters necessary for improving the catalytic efficiency of these materials. The results will have direct impact on the optimal design, performance, and durability of supported catalysts employed in emission treatment; e.g., lean NO_x catalyst, three-way catalysts, oxidation catalysts, and lean NO_x traps, etc.

The typical solid catalyst consists of nano-particles on porous supports. The development of new catalytic materials is still dominated by trial and error methods, even though the experimental and theoretical bases for their characterization have improved dramatically in recent years. Although it has been successful, the empirical development of catalytic materials is time consuming and expensive and brings no guarantees of success. Part of the difficulty is that most catalytic materials are highly non-uniform and complex, and most characterization methods provide only average structural data. Now, with improved capabilities for synthesis of nearly uniform catalysts, which offer the prospects of high selectivity as well as susceptibility to incisive characterization combined with state-of-the science characterization methods, including those that allow imaging of individual catalytic sites, we have compelling opportunity to markedly accelerate the advancement of the science and technology of catalysis.

Computational approaches, on the other hand, have been limited to examining processes and phenomena using models that had been much simplified in comparison to real materials. This limitation was mainly a consequence of limitations in computer hardware and in the development of sophisticated algorithms that are computationally efficient. In particular, experimental catalysis has not benefited from the recent advances in high performance computing that enables more realistic simulations (empirical and first-principles) of large ensemble atoms including the local environment of a catalyst site in heterogeneous catalysis. These types of simulations, when combined with incisive microscopic and spectroscopic characterization of catalysts, can lead to a much deeper understanding of the reaction chemistry that is difficult to decipher from experimental work alone.

Thus, a protocol to systematically find the optimum catalyst can be developed that combines the power of theory and experiment for atomistic design of catalytically active sites and can translate the fundamental insights gained directly to a complete catalyst system that can be technically deployed.

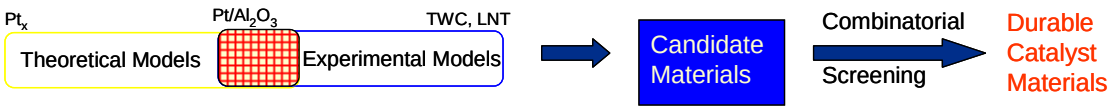

Although it is beyond doubt computationally challenging, the study of surface, nanometer-sized, metal clusters may be accomplished by merging state-of-the-art, density-functional-based, electronic-structure techniques and molecular-dynamic techniques. These techniques provide accurate energetics, force, and electronic information. Theoretical work must be based electronic-structure methods, as opposed to more empirical-based techniques, so as to provide realistic energetics and direct electronic information.

A computationally complex system, in principle, will be a model of a simple catalyst that can be synthesized and evaluated in the laboratory. It is important to point out that such a system for experimentalist will be an idealized simple model catalyst system that will probably model a "real-world" catalyst. Thus it is conceivable that "computationally complex but experimentally simple" system can be examined by both theoretical models and experimental work to forecast improvements in catalyst systems.

Our goals are as follows:

- Our theoretical goal is to carry out the calculation and simulation of realistic Pt nanoparticle systems (i.e., those equivalent to experiment), in particular by addressing the issues of complex cluster geometries on local bonding effects that determine reactivity. As such, we expect in combination with experiment to identify relevant clusters, and to determine the electronic properties of these clusters.
- Our experimental goal is to synthesize metal carbonyl clusters, decarbonylated metal clusters, sub-nanometer metal particles, and metallic particles (~5 nm) on alumina (commercial high surface area, sol-gel processed, and mesoporous molecular sieve), characterize them employing modern techniques including Aberration Corrected Electron Microscope (ACEM), and evaluate their CO, NO_x, and HC oxidation activity.
- This approach will allow us to identify the catalyst sites that are responsible for CO, NOx, and HC oxidation. We will then address support-cluster interaction and design of new durable catalysts systems that can withstand the prolonged operations.

Technical Highlights

Our results on theoretical and experimental work on Platinum-Alumina Systems are summarized in following paragraphs.

Experimental Studies:

2%Pt/γ-Al_2O_3 Catalyst

In our previous report, we described the synthesis and preliminary characterization of 2% Pt/γ–alumina materials. Following subsections describe the detailed structure and nanostructural changes during CO oxidation.

1 nm 2%Pt/γ-alumina - Nano-Structural Changes in Supported Pt Catalysts during CO Oxidation:

The nanostructure of supported Pt catalysts is not well understood. The Z-contrast imaging reports in literature describe the presence of 3-atom clusters and allocate anomalous long Pt-Pt bond to OH terminated Pt clusters. Recent EXAFS studies, on the other hand, suggest thermal metal-metal bond contraction after hydrogen reduction of Pt/γ-Al_2O_3 whose TEM shows particles in 0.5-1.5 nm range centered at ~0.9 nm consisting of 15±9 atoms on average.

Our dark-field STEM imaging of 1 nm Pt/γ-Al_2O_3 shows features identical to those reported previously in terms of particle size distribution. The ACEM HA-ADF STEM images of this catalyst, on the other hand, show that there are single atoms, 2-3 atom clusters, and several 10-20 atom clusters of Pt. The directly measured Pt-Pt bond distances are 2.35, 2.54, 2.7, and 3.2Å for 2-atom clusters, and 2.3, 2.8 Å for 3-atom clusters. These do not match with our theoretical models, perhaps due to projection effects and/or substrate interactions.

The CO oxidation resulted in changes in nano-structure. In order to correlate nanostructural changes with CO oxidation event, we stopped the reaction at CO oxidation initiation and CO oxidation completion (the CO conversion efficiency as a function of temperature was described in the previous report).

a. The CO oxidation reaction was stopped once it reached 4.1% conversion at 210ºC and the catalyst sample was collected. It was loaded on a TEM sample grid by dry-dipping. STEM imaging indicates an average Pt size of 1.9 nm with the clusters/particles ranging in size from 0.7-3.8 nm, see Figure 1. Figure 2 compares the particle size distribution of the initiation used catalyst with that seen for the fresh catalyst.

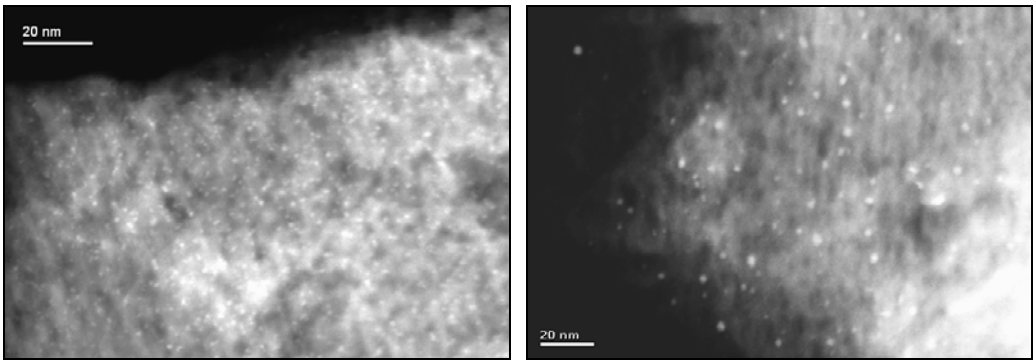

Figure 1. STEM images of fresh 1nm 2%Pt/γ-alumina (left) and after CO oxidation initiation testing (right). Both images show 20 nm scale bars.

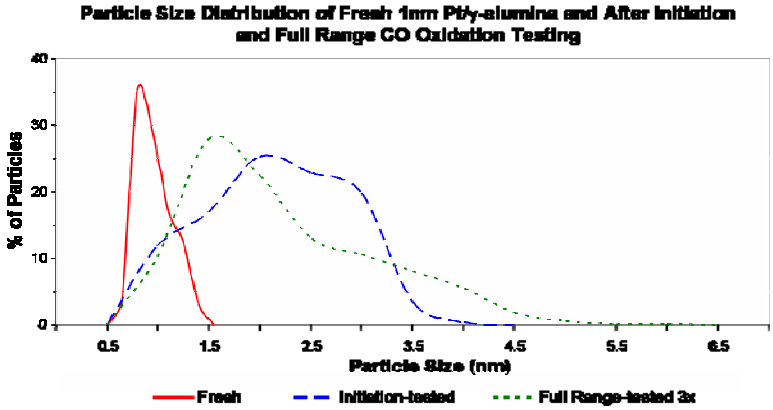

Figure 2. Particle size distribution comparison of 1 nm 2%Pt/γ-alumina catalyst according to STEM imaging of multiply areas, for fresh and CO oxidations tested samples (initiation and full range 3x). Sizes have been sorted into ranges for this graph and all begin and end at zero.

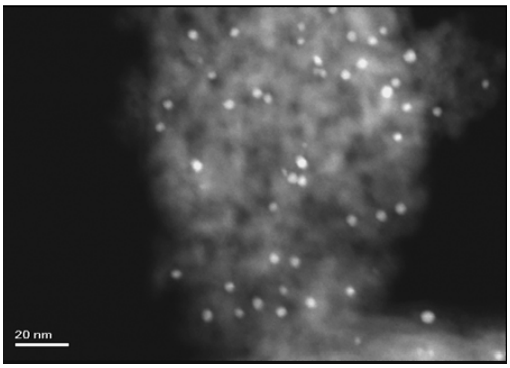

Figure 3. STEM images of 1 nm 2%Pt/γ-alumina after three cycles of quantitative CO oxidation (the scale bar is 20 nm).

b. The CO oxidation reaction was allowed to attain quantitative conversion and then the reaction was stopped and reactor was cooled. The reaction was restated and allowed to attain quantitative CO oxidation. After a third cycle, the catalyst sample was collected. STEM imaging of multiple areas indicates an average Pt size of 2.0 nm but range from 0.7-5.6 nm [Figure 3]. Figure 2 shows the particle size distribution that appears to be bimodal. The distribution of smaller particles is centered at 1.5 nm while that of the larger ones at 3.5 nm.

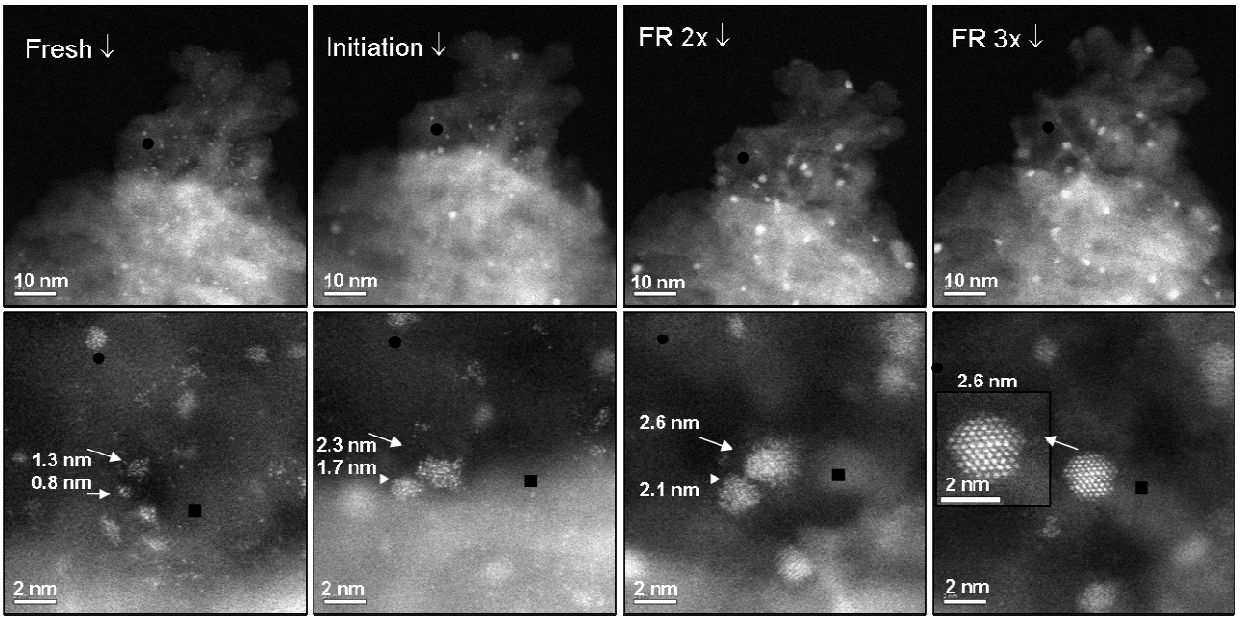

Figure 4. ACEM HAADF-STEM images of the exact same sample area: Fresh 2%Pt/γ-Al_2O_3 and after Initiation testing, Full Range 2x and Full Range 3x (left to right, respectively). The white dots are Pt atoms and grey area is the alumina support. The second row shows the area at higher magnification for each stage, respectively. Circles and squares are located at the same place on each image to allow monitoring of Pt growth at each stage of testing.

The nano-structural changes seen at the initiation and at the end of three CO-oxidation cycles led us to investigate this catalytic reaction employing ORNL *ex-situ* reactor. As described

previously, the ex-situ reactor allows us to expose catalyst samples on a TEM grid to various catalyst operating conditions and the structural changes then can be repeatedly monitored in selected areas by electron microscopy. The fresh sample was exposed to the following operating conditions (1) CO oxidation initiation conditions, (2) Quantitative CO oxidation – 2 cycles, and (3) Quantitative CO oxidation – 3 cycles. The fresh sample showed small Pt clusters and single Pt atoms (Figure 4). The same spots in multiple areas were monitored by ACEM after exposure to the above mentioned conditions. Atomic resolution electron imaging of the sample after 2 cycles of quantitative CO oxidation shows that the Pt cluster/particles have sintered significantly and only a very few clusters around the 1 nm size can now be seen (Figure 4, FR 2x). The larger particle surprisingly did not exhibit any atomic order; however, in other sample areas after 2 cycles of quantitative CO oxidation atomic ordering was seen. After 3 cycles of quantitative CO conversion, the number of larger Pt clusters/particles increased further. These Pt particles typically exhibited well ordered structures as can be seen in Figure 4.

25 nm 2%Pt/γ-alumina:

Imaging of multiple areas of a TEM sample grid containing the 2%Pt/γ-Al_2O_3 annealed at 650ºC/5 h by STEM confirmed the presence of Pt particles ranging from 3.4 to 36.7 nm (larger outlier at 138.1 nm also seen). The average particle size for the Pt (excluding the outlier) seen by electron microscopy was 12.9 nm, see Figure 5 (left).

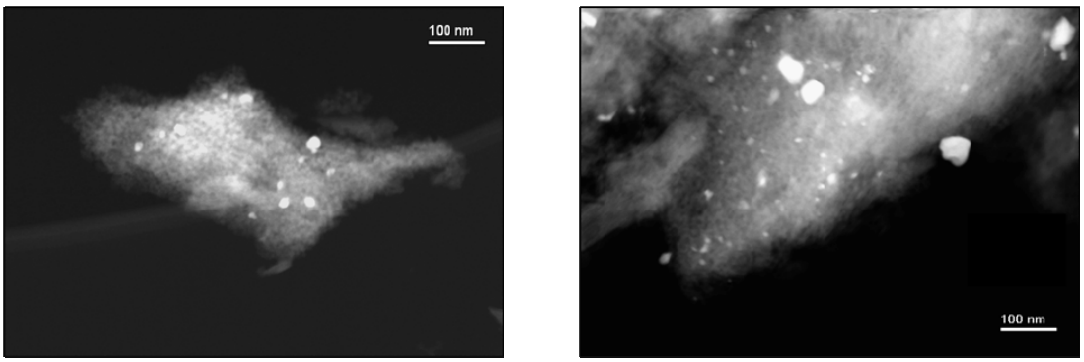

Figure 5. STEM images of fresh 25 nm 2%Pt/γ-alumina (left) and after CO oxidation initiation testing (right). Both images show 100 nm scale bars.

The CO oxidation on 25 nm 2%Pt/γ-alumina also resulted in Pt particle sintering under various catalyst operating conditions:

a. The CO oxidation over 25 nm 2%Pt/γ-alumina catalyst in catalytic reactor was allowed to achieve 8.1% conversion at 240ºC (CO oxidation initiation) and reaction was stopped. The catalyst sample was collected after cooling and deposited on TEM grid by dry dipping. STEM imaging indicates an average Pt size of 13.1 nm with the particles ranging in size from 1.4-87.9 nm, see Figure 5 (right). Figure 6 compares the particle size distribution of the initiation used catalyst with that seen for the fresh catalyst

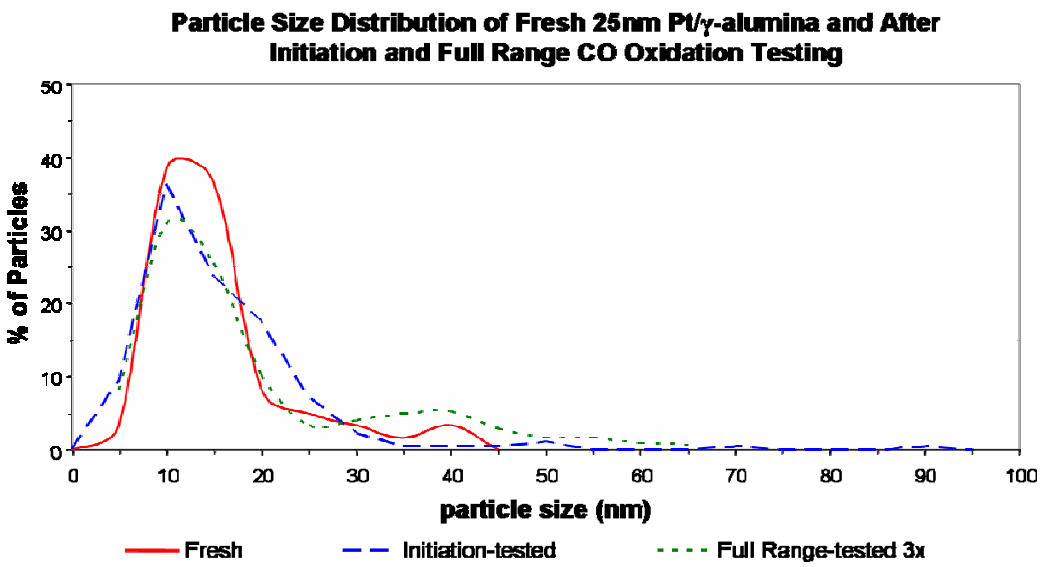

Figure 6. Particle size distribution comparison of 25 nm 2%Pt/γ-alumina catalyst according to STEM imaging of multiply areas, for fresh and CO oxidations tested samples (initiation and full range 3x). Sizes have been sorted into ranges for this graph and all begin and end at zero.

b. The CO oxidation over fresh 25 nm 2%Pt/γ-alumina was allowed to reach quantitative conversion and the reaction was stopped and the reactor was cooled before restarting. After a third cycle of achieving quantitative CO oxidation at 242°C, the reactor was cooled and catalyst sample was collected. STEM imaging of multiple areas indicates an average Pt size of 17.0 nm but range from 1.7-68.7 nm. The increase in the average particle size compared to that seen after initiation testing can be seen in Figure 7. Figure 6 compares this particle size range and the quantity of larger particles with that seen for the fresh and initiation tested samples.

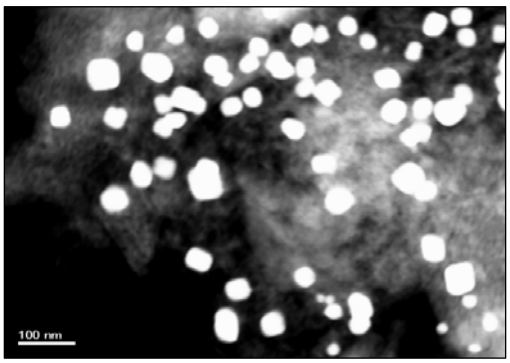

Figure 7. STEM image of 25 nm 2%Pt/γ-alumina after 3 cycles of quantitative CO oxidation (the scale bar is 100 nm).

Table 1 summarizes the Pt particle sizes observed after the catalysts have been subjected to various stages of CO oxidation. These results suggest the following:

- A gradual increase in the average Pt size and the quantity of larger particles/cluster is seen for 2%Pt/γ-alumina catalysts. The initial particle size (1 nm or 25 nm) is not a predictor of extent of sintering.
- ACEM studies show that larger particles formed as a result of sintering should not be assumed to be ordered metallic particles.

- Lattice spacing measurements of atomic resolution electron imaging of ordered Pt particles suggest that after CO oxidation over 1 nmPt/γ-alumina catalyst, Pt-oxides are present. In Figure 4, the inset image on row two for FR 3x is a bcc Pt_3O_4 particle looking down the (120) lattice plane.

Table 1. Average Pt particle size and ranges seen by STEM before and after CO oxidation testing.

	Fresh	**Initiation**	**Full Range 3x**
1nm Pt/γ-alumina	0. 9 nm (0.6-1.4 nm)	1.9 nm (0.7-3.8 nm)	2.0 nm (0.7-5.6 nm)
25nm Pt/γ-alumina	12.9 nm (3.4-36.7 nm)	13.1 nm (1.4-87.9 nm)	17.0 nm (1.7-68.7 nm)
1nm Pt/θ- sg alumina			
25nm Pt/θ- sg alumina			

Next Steps: We plan to carry out the following tasks:

- We plan to complete CO oxidation studies of already synthesized Pt clusters on alumina and MgO to determine the metal species involved in CO oxidation. The results will be compared with the results from theoretical calculation. If consistent, we will proceed with the evaluation of the catalysts for NO_x and hydrocarbon oxidation.

- We will synthesize Pt clusters on sol-gel and molecular sieve alumina. This will create a matrix of samples with varying Pt particles size and oxidation on alumina substrates with increasing surface area and pore structure. We will carry out CO, NO_x and HC oxidation on these samples to study the effect of morphological changes in substrates leading to changes in metal substrate interactions.

- We will continue to investigate the thermochemistry of CO and NO oxidation on free Pt and Pt oxide clusters as well as the properties of Pt and Pt oxide clusters supported on metal oxides (include magnesia and alumina). These investigations will help us gain a better understanding of the structural and catalytic properties of the supported Pt clusters and identify the effect of the support on these important properties.

- We will initiate efforts to employ this approach towards designing a new Lean NO_x catalyst or a combination of catalyst systems that can reduce NO_x in the full operating range of diesel engines.

<u>Publications/Presentations</u>

1. Narula, C. K., Moses, M.J., Xu, Y., Blom, D.A., Allard, L.F., Shelton, W.A. "Catalysis by Design – Theoretical and Experimental Studies of Model Catalysts." *SAE no. 2007-01-1018*, 2007.

2. Narula, C. K., Moses, M.J., Allard, L.F. "Analysis of Microstructural Changes In Lean NO_x Trap Materials Isolates Parameters Responsible for Activity Deterioration" *SAE no. 2006-01-3420*, 2006.
3. Narula, C.K., Moses, M.J. (speaker), Allard, L.F. "Analysis of Microstructural Changes In Lean NO_x Trap Materials Isolates Parameters Responsible for Activity Deterioration." Society of Automotive Engineers Powertrain and Fluid Systems Conference, Toronto, Canada, October 2006.
4. Narula, C. K., Moses, M.J., Allard, L.F. "Analysis of Microstructural Changes In Lean NO_x Trap Materials Isolates Parameters Responsible for Activity Deterioration." SAE 2007 World Congress, Detroit, MI, April 2007. (abstract accepted)
5. Narula, C. K., Moses, M.J., Blom, D.A., Allard, L.F. "Nano-Structural Changes in Supported Pt Catalysts during CO Oxidation." North American Catalysis Society Meeting, Houston, TX, June 2007. (abstract submitted)

Mechanical Reliability of PZT Piezo-Stack Actuators for Fuel Injectors

A. A. Wereszczak and H. Wang
Ceramic Science and Technology (CerSAT)
Oak Ridge National Laboratory

Objective/Scope

The use of piezoelectric stack actuators as diesel fuel injectors has the potential to reduce injector response time, provide greater precision and control of the fuel injection event, and lessen energy consumption (e.g., for use in homogeneous charge compression ignition, HCCI, engines). Though piezoelectric function is the obvious primary function of lead zirconate titanate (PZT) ceramic stacks for fuel injectors, their mechanical reliability can be a performance and life limiter because PZT is both brittle, lacks high strength, and may exhibit fatigue (i.e., slow crack growth) susceptibility. That brittleness and relatively low strength can be overcome with proper design though. This project combines in-situ micromechanical testing, microstructural-scale finite element analysis, probabilistic design sensitivity, and structural ceramic probabilistic life prediction methods to systematically characterize and optimally design PZT piezoelectric stack actuators that will enable maximized performance and operational lifetime.

Technical Highlights

Two commercially available materials were evaluated during the present reporting period and they were 5A4E and PSI 5H4E (Piezo Systems, Inc., Cambridge, MA). 5A4E has a higher coercive field (E_c) and a higher Curie temperature (T_c) than 5H4E, while its piezoelectric coefficient (d_{33}) is lower. 5A4E has a high T_c value of 350°C and is considered to be an excellent candidate for diesel fuel injector systems.

As-received sheets of the two PZT materials having dimensions of 72.4 x 72.4 x 0.27 mm were Ni-electroded and fully poled by the manufacturer. These sheets were cut into small size plates (Bomas Specialty Machining, Somerville, MA) for ball-on-ring (BoR) strength tests. A total of 49 square specimens obtained from each sheet with a nominal size of 10 x 10 mm.

The experimental set-up is a BoR having integrated high voltage application capability. The system is shown in Fig. 1. The bottom centerpiece is a steel-supporting ring (sized with 7.4 mm ID, 25.4 mm OD and 6.35 mm thickness) with a high voltage cable attached. This support ring serves as an electrode and rests on (electrically insulating) alumina plate. On the top of the support ring, the 10 x 10 mm PZT specimen is placed. Above the specimen is a loading steel ball with 2.0 mm diameter and that also serves as the other electrode. The loading ball is mounted onto the bottom of a steel spindle using conductive resin (TIGA Silver 901, Resin Tech, S. Easton, MA). Above the spindle are an electrically insulating polymer adapter and a 1000 g load cell. The (vertical) Z-direction loading action was controlled by a stepper motor, and works in displacement-controlled mode with a crosshead speed of 0.001 mm/s. The other two stepper motors control X and Y coordinates of the base. Therefore, the alignment of the loading axis with the supporting (ring) axis is controllable within several micrometers. The mounting process of the PZT specimen onto the supporting ring is also monitored with a TV screen through a video camera. The control and calibration of system and data acquisition are controlled using LabView software (NI, Austin, TX). The high voltage (HV) cable and the ground wire are

connected onto their respective terminals of a high voltage amplifier (Trek model 609E-6, Medina, NY) that is powered by a DC power supply.

A total of four combinations of electro-mechanical loading were tested in this study. The first two correspond to an open circuit (OC) with the positive electrode of specimen in tension (PoT) and with the negative in tension (NoT), and the second pair correspond to the high electric field with the PoT and the NoT. The existing electrical field in the OC is typically low, and therefore, the first two combinations would exploit any surface condition effect on strength (if it exists), but not the electrical field effect. With a high electric field (E) applied, a positive E was actually generated in the PoT, and a negative E was generated in the NoT due to the configuration of the set-up. In each case of the latter two combinations, the level of E applied was the respective coercive field E_c of each tested PZT material; namely, 1.2 kV/mm for 5A4E and 0.8 kV/mm for 5H4E. For each of four combinations, nine to fifteen specimens were tested to detect a statistically significant effect for a specific PZT. For the 5H4E, remnant specimens from a previous period of our project were also tested because it was found that the strength of one sheet exhibited substantial differences.

The failure of the poled PZT plate was not catastrophic and its loading curve exhibited multiple peaks. The test was interrupted in order to inspect the damage sequences associated with those peaks. Both optical (Nikon Nomarski Measure Scope MM-11, Tokyo, Japan) and SEM (Hitachi S4100 field emission scanning electron microscope, San Jose, CA) were used to examine the recovered plate after the first peak. In most cases, the optical microscope was capable of catching the primary crack on the tensile side of the recovered plate. However, there were circumstances in which both optical microscope and SEM failed to reveal that cracking. Therefore, to study this further the Ni-electrode was removed from the plate for further examination using a chemical solution of 75% nitric acid + 25% water for 1.5 hours; this revealed the crack on the tension side of the specimen. As a result of this investigation, the load at the first peak was thereafter taken as the failure load of the material and used in the calculation of biaxial strength.

The strength data set for each loading condition was subsequently analyzed using Weibull statistics software (WeibPar, Connecticut Reserve Technologies, Inc., Strongsville, OH). The software estimated Weibull modulus (m) and characteristic strength (σ_θ) and their confidence intervals. Unbiased maximum likelihood parameter estimation was employed for these parameters.

Results

The strength results of all the specimens cut from 5A4E Sheet 3 are shown in Fig. 2. In the left column [Fig. 2(a)] are those with the OC condition where the upper is the data set for the PoT and the lower for the NoT. For each electro-mechanical load case, the WeibPar output is also given in Fig. 2(a) along with the parameters used in the test, including characteristic strength and Weibull modulus and corresponding 95% confidence intervals. As seen, these two data sets are essentially overlaid, and therefore, the strength of this material was independent of which side was loaded in tension.

In the right column [Fig. 2(b)] is the specimen strength data from same sheet (Sheet 3) with concurrently applied electrical field. Under a positive E, the characteristic strength was found to be 158 MPa and that was statistically significantly higher than that of the OC. Under a negative E, the characteristic strength was 116 MPa and statistically lower than that of the OC. Consequently, a positive electric field enhances the strength and a negative one reduces it. The Weibull modulus in each of the cases was slightly lower; however, this was not significant.

As mentioned above, both the data sets of PoT and NoT under the OC were not different so their data were pooled. The pooled data set was input into WeibPar and the parameters re-estimated. The confidence rings of estimates (with Weibull modulus in abscissa and characteristic strength in ordinate) for three cases are illustrated in Fig. 3. The lower ring is for E = -1.2 kV/mm, the middle one is for the OC, and the upper one for E = 1.2 kV/mm. The trend shows the ring shifts downwards under a negative field, and upwards under a positive field. These shifts in strength distributions are statistically significant.

For 5H4E, the confidence ring now shifts down and left under E = -0.8 kV/mm and up and right under E = 0.8 kV/mm. These shifts are statistically significant. This observation indicates that not only characteristic strength changes, but also Weibull modulus exhibits a similar tendency.

Because strength significantly decreased due to the negative electrical field, the case of $E = -E_c$ became the focus of the fractographical study of both PZT materials.

The image on the fracture surface in Fig. 4 (a) was taken for a 5A4E specimen with E = -1.2 kV/mm and that had an intermediate strength. The bottom of the cross section was the tension side of bending. An arch pattern shows up in the background that consists of many arch ledges and that laterally spreads. These ledges converge into the failure origin on the tension side. The arrows delineated the size and shape of failure origin. It was difficult to classify the observed flaw, but we believe it could be appropriately designated as a surface-type processing flaw. The enlarged view on the failure origin, in Fig. 4 (b), revealed the prevailing transgranular fractures. In fact, it is the adjoining transgranular fractures that form the ledges in the background. On the other fracture surfaces (not shown), the cracked grained boundaries, volume pores and surface voids were observed within or around the failure origin. Overall, the EDS did not reveal any significant chemical difference between the failure origin and the background.

For 5H4E sheet 3, prevailing intergranular fracture was revealed on the fracture surface. Because of that, the change of topographical features between the background and the failure origin on the tensile edge becomes quite subtle. The SEM image illustrated that the ledges on the fracture surface were not as distinct as those in 5A4E. However, the surface-type processing flaw is still identified as the type of failure origin.

Parallel work is ongoing to construct a piezostack test facility and that progress will be reported on in the next Quarterly Report.

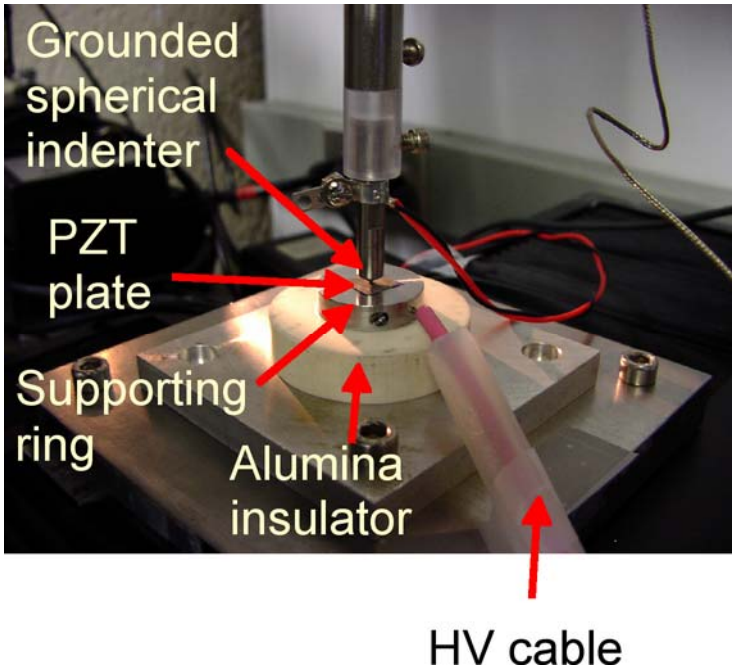

Figure 1. Experimental set-up details for superimposed mechanical and electric field testing. The HV (high voltage) cable and ground wire are connected into a HV amplifier that is not shown.

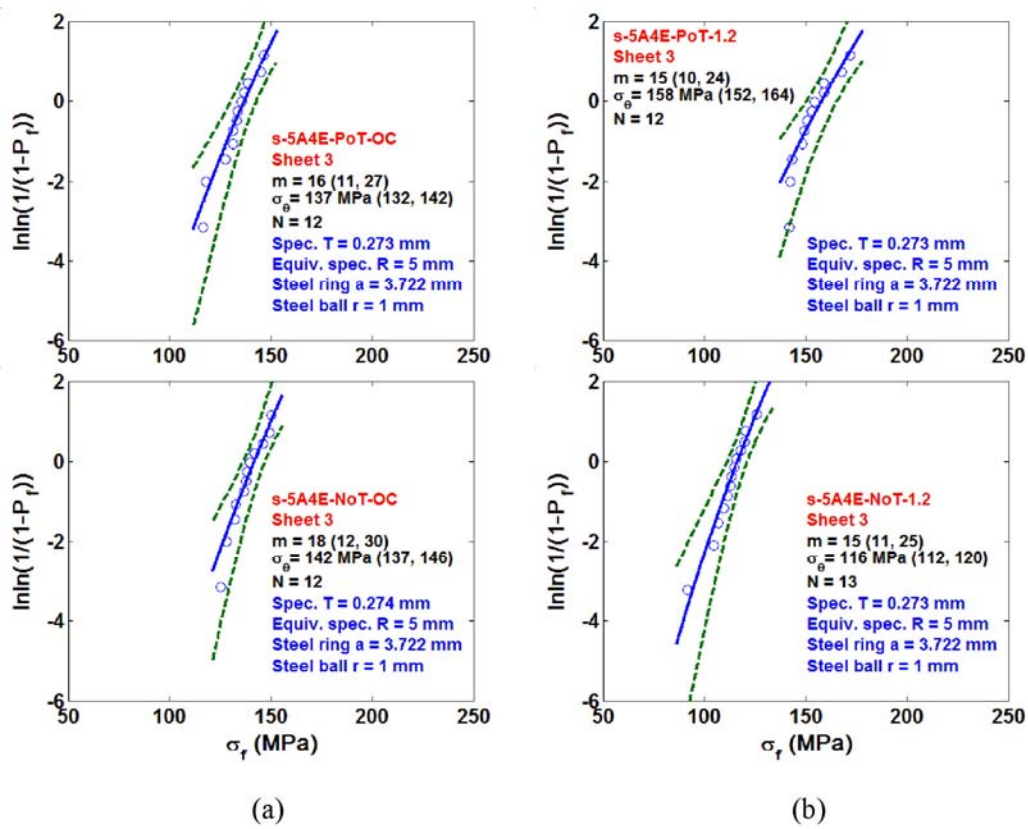

(a) (b)

Figure 2. Weibull analysis results for 5A4E; (a) PoT (upper) and NoT (lower) under OC condition, and (b) for E = 1.2 kV/mm (upper) and -1.2 kV/mm (lower).

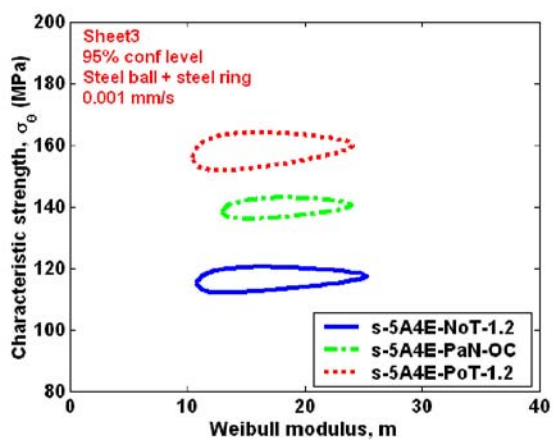

Figure 3. Confidence rings for 5A4E. The confidence ring s-5A4E-PaN-OC represents the data set pooled for square plates of 5A4E with PoT and NoT under OC.

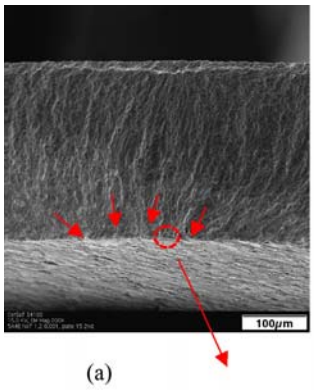

(a)

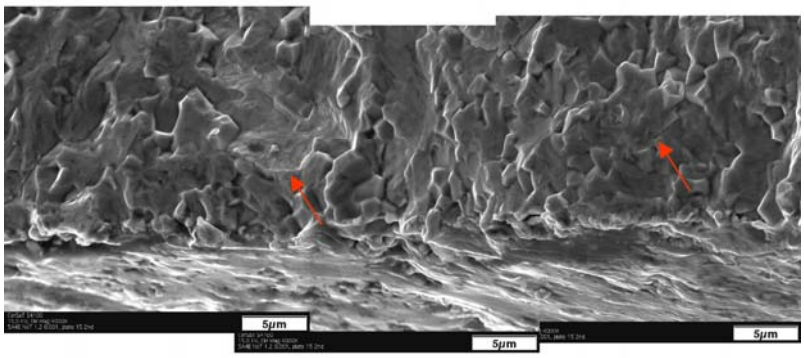

(b)

Figure 4. Fracture surface of 5A4E for E = -1.2 kV/mm and σ_f = 114.7 MPa. (a) Cross section of fracture surface whose failure origin is delineated by the arrows, (b) the enlarged area into the failure origin where transgranular fracture prevailed.

Status of FY 2006 Milestones

Establish piezoactuator reliability test facility. [09/07] *On schedule.*

Communications/Visits/Travel

Separate discussions held with Caterpillar, EPCOS, Noliac, and Penn State University about our PZT actuator work.

Publications

H. Wang and A. A. Wereszczak, "Effects of Electric Field on the Biaxial Strength of Poled PZT," to be submitted to *Ceramic Engineering and Science Proceedings*.

References

None.

Advanced Cast Austenitic Stainless Steels for High Temperature Components

P. J. Maziasz, John P. Shingledecker, and N. D. Evans
Oak Ridge National Laboratory

M. J Pollard
Caterpillar, Inc.

Objective/Scope

This is the 2nd ORNL CRADA project with Caterpillar. This CRADA project is focused on commercialization of the new CF8C-Plus cast austenitic stainless steel, which was developed during the first ORNL/CAT CRADA. CF8C-Plus stainless steel is a cost-effective material upgrade for much more performance, durability and temperature capability relative to current heavy-duty diesel engine exhaust components made from SiMo ductile cast iron. In FY2005, this project completed the initial properties data base needed for alternate materials selection, and component design or redesign, including fatigue, thermal fatigue, and creep, and studies of aged materials. In FY2006, longer term creep-testing and fatigue studies at much lower frequencies were completed, together with new tests directly related to specific new component applications, like turbocharger housings. This CRADA (Cooperative Research and Development Agreement) project (ORNL02-0658) was extended beyond the initial 3-year term last year, and will be completed in July, 2007. Requests for more detailed information on this project should be made directly to Caterpillar, Inc.

Highlights

Caterpillar, Inc.

Caterpillar obtained the U.S. Patent 7,153,373 B2 on December 26, 2006 for "Heat and Corrosion Resistant Cast CF8C Stainless Steel with Improved High-Temperature Strength and Ductility." Caterpillar and ORNL are working together to obtain an ASTM alloy designation for CF8C-Plus stainless steel. The Caterpillar Regeneration System (CRS) components are currently being produced from CF8C-Plus steel for on-road engine applications begin in 2007. Caterpillar is in discussions with turbocharger manufacturers for licensing CF8C-Plus steel.

ORNL

ORNL placed a subcontract with Stainless Foundry & Engineering (SF&E, one of the three current trial-licensees) to produce castings of CF8C-Plus and to do appropriate testing for ASTM Weld Procedure Qualification, to evaluate the weldability and fluidity of CF8C-Plus Cu/W relative to CF8C-Plus. SF&E also produced step castings of both CF8C-Plus and –Plus Cu/W to evaluate the properties of thin-section casting relevant to turbocharger housings.

Technical Progress

Background

Current cast iron heavy diesel engine exhaust manifolds and turbocharger housings are being pushed beyond their temperature capabilities as normal duty cycles approach or exceed 750°C; the rapid and severe thermal cycling contributes to increased failures. The new cast CF8C-Plus

austenitic stainless steel has now been commercialized, and business opportunities are being pursued and supported for this and other high-temperature applications. Caterpillar, Inc. and ORNL have completed the systematic and thorough properties data base required by designers to optimize component design, and are currently characterizing the properties of trial or prototype commercially cast stainless steel components.

Approach

Multiple commercial heats of CF8C-Plus have been cast by several commercial foundries, including static sand and centrifugal casting methods. Now, both large and small prototype CF8C-Plus components have been cast. In July 2004, a large turbine housing for an industrial gas-turbine was cast by MetalTek, International, Inc. from an 8000 lb heat of the new CF8C-Plus stainless steel. In 2005, three foundries obtained trial-licenses for CF8C-Plus steel, including MetalTek and Stainless Foundry & Engineering. By the end of 2005, over 31,000 lb of CF8C-Plus components have been cast, including exhaust manifolds, and some new, thin-walled piping. In 2005, new commercial heats of CF8C-Plus Cu/W were made, and in 2006 found to have more tensile strength and more creep resistance than CF8C-Plus at 750°C and above. In July, 2006, Caterpillar chose CF8C-plus to use for the Caterpillar Regeneration System burner housing that will be included on all highway heavy-duty truck diesel engines in 2007.

Technical Progress – Caterpillar, Inc.

After completing prototyping and testing, Caterpillar is implementing the new cast CF8C-Plus stainless steel as the body casting for the Caterpillar Regeneration System (CRS) for on-highway truck diesel engines, beginning in 2007. The CRS device burns diesel fuel in the exhaust stream to heat the diesel particulate filter, in order to oxidize soot and regenerate the filter. This component is subject to extreme temperatures and thermal cycling, which makes the CF8C-Plus stainless steel a durable and relatively low-cost choice for this application.

This quarter, Caterpillar continued discussions with turbocharger manufacturers for use and licensing of CF8C-Plus cast stainless steel for turbocharger housings.

Technical Progress – ORNL

ORNL placed a subcontract last quarter with Stainless Foundry & Engineering (SF&E, one of the three current trial-licensees) to produce castings of CF8C-Plus and to do appropriate testing for ASTM Weld Procedure Qualification, to evaluate the weldability and fluidity of CF8C-Plus Cu/W relative to CF8C-Plus.

CF8C-Plus was found to be weldable, consistent with several prior weld-trials, and the data needed for ASTM Weld Procedure Qualification was obtained. Relative comparison of the new CF8C-Plus Cu/W showed it to also have similar weldability and similar good metal fluidity compared to the standard CF8C-Plus steel.

SF&E also produced step castings of both CF8C-Plus and –Plus Cu/W to evaluate the properties of thin-section casting directly relevant to turbocharger housing components. 24 step-cast ingots were received at ORNL in December, 2006 for further evaluation, 12 of the standard CF8C-Plus steel and 12 of the new CF8C-Plus Cu/W steel.

Communications/Visits/Travel

Detailed team communications between ORNL and Caterpillar occur regularly. The new 3 year CRADA began on July 21, 2002, when the previous CRADA ended and is scheduled to end on July 21, 2005. The two-year ORNL/Caterpillar CRADA extension was done last year until July 21, 2007.

ORNL hosted a visit from GE Energy, Greenville, SC on October 24, 2006, and discussions included an update on the properties and patent/technology transfer status of cast CF8C-Plus austenitic stainless steel.

Status of Milestones (ORNL for DOE)

Test properties of prototype components made of CF8C-Plus or –Plus Cu/W in support of diesel exhaust components, or other parts made by trial-licensee foundries for commercial applications (May, 2007). On-track for completion.

Publications/Presentations/Awards

Patents:

U.S. Patent 7,153,373 B2 on "Heat and Corrosion Resistant Cast CF8C Stainless Steel With Improved High Temperature Strength and Ductility," by P. J. Maziasz, T. McGreevy, M. J. Pollard, C. W. Siebenaler, and R. W. Swindeman, was obtained on December 26, 2006.

U.S. Patent Application 11/495,671 on "Heat and Corrosion Resistant Cast Austenitic Stainless Steel Alloy with Improved High Temperature Strength," by P. J. Maziasz, M. J. Pollard, and J. P. Shingledecker was filed on July 31, 2006.

Publications:

None.

Presentations:

"Design and Evaluation of New High-Temperature Stainless Steels and Alloys" was given by P. J. Maziasz at a meeting with GE-Energy at ORNL on Oct. 24, 2006.

"Development and Application of CF8C-Plus," was given by J. P. Shingledecker (P. J. Maziasz, N. D. Evans, M. L. Santella, and M. J. Pollard, co-authors) at a meeting with GE-Energy at ORNL on Oct. 24, 2006.

Friction and Wear Reduction in Diesel Engine Valve Trains

Peter Blau and Jerry McLaughlin
Oak Ridge National Laboratory

Objective/Scope

The objective of this effort is to enable the selection and use of improved materials, surface treatments, and lubricating strategies for value train components in energy-efficient diesel engines. Depending on engine design and operating conditions, between 5 and 20% of the friction losses in an internal combustion engine are attributable to the rubbing between valve train components. Wear and consequent leaks around valve seats can reduce cylinder pressure and engine efficiency. Contacting surfaces in the valve train include the valve heads, seats, tappets, guides, and stems. This effort is designed to address key rubbing interfaces within the valve train where there are opportunities to employ advanced materials and surface treatments to reduce friction and save energy.

A two-pronged, interdisciplinary approach is planned to address both materials and lubrication-related aspects. The first task concerns the design and construction of a laboratory testing apparatus to simulate the thermal, chemical, and mechanical contact environment characteristic of valves and valve seats. A second task involves improving the performance of the valve stems as they oscillate within the valve guides. The latter takes into consideration not only the selection of stem and guide materials, but also the characteristics of thin lubricant films and the micromechanics of the moving surfaces. Therefore, this project embodies surface science and tribology to solve practical engineering challenges.

Technical Highlights

Design of a High-Temperature, Controlled Environment, Valve Material Testing System. Construction and preliminary testing of a controlled-environment, repetitive-impact system is nearly complete. The High-Temperature Repeated Impact (HTRI) apparatus will be a tool to investigate the durability of candidate exhaust value materials, identifying their primary modes of surface damage and providing guidance for the selection of new bulk materials, coatings, and surface treatments for use in engines that burn a variety of fuels.

In the last quarter, construction was completed on the oscillating drive assembly. The general features of the HTRI are shown schematically in Figure 1(a). The specimen holder to fit a production exhaust valve, shown in Figure 1(b), was installed and the furnace was successfully heated to 900° C for several hours. Most tests of exhaust valve materials will likely be conducted at or below 850° C to simulated maximum expected diesel engine operating temperatures. A quartz tube was obtained to act as an environmental chamber, and water-cooled upper and lower flanges were designed, installed, and tested. Initial tests will be conducted during the next quarter to ensure proper specimen alignment and the correct functioning of the mechanical system when the fixtures are heated and repetitive impact conditions are imposed.

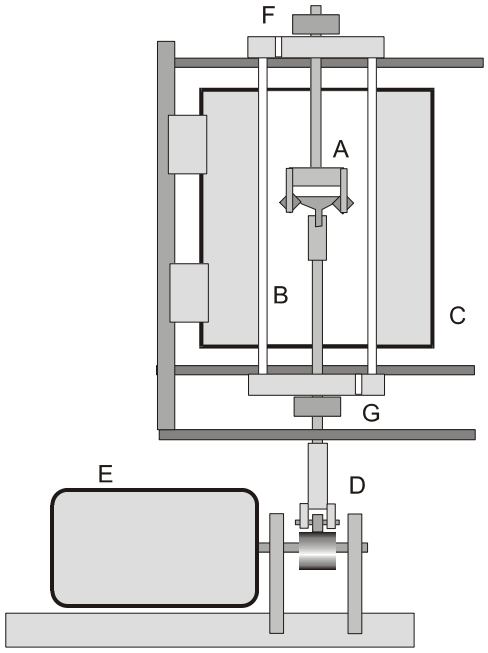

(a)

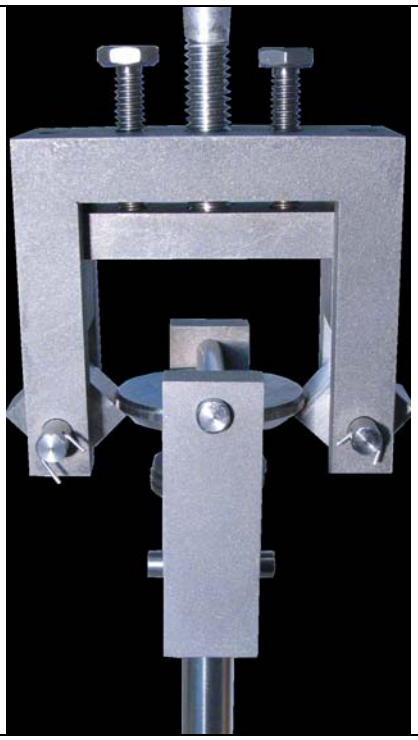

(b)

Figure 1. (a) Schematic representation of the HTRI apparatus showing, the motor drive (D, E), the test specimen fixture (A), the quartz chamber (B), the tube furnace (C), and gas fittings (F,G) through water-cooled flanges. (b) Specimen holder showing a diesel engine exhaust valve in contact with two test blocks that will simulate the seat material.

Future Plans

1) Complete construction of the HTRI and conduct preliminary elevated temperature tests on conventional exhaust valve materials.
2) Working with an engine manufacturer, obtain samples of diesel engine valves that were run in fired engines and compare wear damage to that generated in the HTRI.

Travel

None

Status of Milestones

1) Complete first matrix of tests to compare traditional and advanced valve/valve seat materials at high temperature, in controlled-atmosphere, and with repetitive impact conditions. Submit report or journal article on the results. **(03/07)**
2) Prepare an analysis of the basic mechanisms that operate as valve/valve seat materials degrade in service and correlate them with basic material properties and metallurgical structure. Submit report or journal article describing the analysis. **(09/07)**

Publications and Presentations

None.

Lightweight Valve Train Materials

Nathaniel S. L. Phillips
Caterpillar Inc.

Introduction

Valve train components in heavy-duty engines operate under high stresses and temperatures, and in severe corrosive environments. In contrast, the valve train components in the light-duty engine market require cost-effective reliable materials that are wear resistant and lightweight in order to achieve high power density. For both engine classes, better valve train materials need to be identified to meet market demand for high reliability and improved performance, while providing the consumer lower operating costs.

Advanced ceramics and emerging intermetallic materials are highly corrosion and oxidation resistant, and possess high strength and hardness at elevated temperatures. These properties are expected to allow higher engine operating temperatures, lower wear, and enhanced reliability. In addition, the lighter weight of these materials (about 1/3 of production alloys) will lead to lower reciprocating valve train mass that could improve fuel efficiency. This research and development program is an in-depth investigation of the potential for use of these materials in heavy-duty engine environments.

The overall valve train effort will provide the materials, design, manufacturing, and economic information necessary to bring these new materials and technologies to commercial realization. With this information, component designs will be optimized using computer-based lifetime prediction models, and validated in rig bench tests and short-and long-term engine tests.

Program Overview

Information presented in this report is based on previous proprietary research conducted under Cooperative Agreement DE-FC05-97OR22579.

Ceramic Materials

Silicon nitride materials have been targeted for valve train materials in automotive and diesel industries since the early 1980's. Some silicon nitride (Si_3N_4) material grades have reached a mature level of materials processing, capable of being implemented into production. Commercial realizations have been reported in both automotive and diesel valve trains, with large-scale production underway. The Si_3N_4 valve train components in production are used in high rolling contact stress applications and have exhibited superior wear resistance and longevity.

Intermetallic Materials

Titanium aluminide (TiAl) based intermetallics retain their strength at elevated temperature and are highly corrosion-resistant. They are lightweight and possess high fracture toughness. These alloys are actively being investigated for several aerospace and automotive applications.

Twentieth Quarter Summary

The primary focus of this quarter is the analysis of the valves subjected to the first 500-hour durability test on the Caterpillar natural gas G3406 genset. In this quarter, the analysis of the valves from the first 500 hours of engine exposure has been achieved. Table 1 outlines the progress of this engine durability test.

Table 1. Engine durability test progress

Phase	Action	Status
Initial Installation	Valve Install	Complete March
Phase #1 (0 h – 100 h)	Engine Exposure	Complete May
	Post-test Analysis	Complete June
Phase #2 (100 h – 500 h)	Engine Exposure	Complete July
	Post-test Analysis	Complete November
Phase #3 (500 h – 1000 h)	Engine Exposure	Not yet started
	Post-test Analysis	Not yet started

This quarterly report will document the preliminary observations noted during Phase #2 and will discuss the plans and expected results from the remainder of the test.

Engine operating conditions

The valves were installed in the following arrangement (Table 2) to ensure that the performance of the Si_3N_4 and TiAl valves could be isolated for analysis.

Table 2. Valve installation arrangement

Cylinder	Intake	Exhaust
1	Silicon Nitride	Silicon Nitride
2	Silicon Nitride	Silicon Nitride
3	Silicon Nitride	Titanium Aluminide
4	Production Steel	Titanium Aluminide
5	Production Steel	Production Steel
6	Production Steel	Production Steel

The genset was operated at 125 kW, approximately half of rated conditions, for the majority of the test due to a knocking phenomenon described in past reports. All Si_3N_4 and TiAl valves were removed from the genset after 500 hours of testing and prepared for non-destructive analysis.

Valve Inspection – Non-Destructive Analysis

In a heavy-duty engine, the first 100 hours of operation time is considered the "break-in" period. During this initial phase the valve seat and seat insert typically conform to each other, resulting in scuffing of the valve seat. Valve/guide contact may also cause break-in wear on the stem and valve/bridge contact may cause stem tip wear. After the initial 100 hours, the wear will continue to increase, although at a slower rate, before eventually reaching a steady state where minimal wear is observed. With the TiAl and Si_3N_4 valves there was minimal stem tip wear, acceptable valve/guide wear but significant seat/insert wear after the first 100 hours. Similar results were seen after 500

hours, except the seat/insert wear was slightly worse. Figures 1a shows a representative Si_3N_4 exhaust valve (Si3N4E-32) after 100 hours as it was positioned in the cylinder, while Figure 1b shows the valve after 500 hours of test engine time. As expected, there is an even coating of combustion byproduct on the head face, fillet and lower valve stem region. The stem wear is evident in the discoloration that ends halfway up the valve. Figures 2a-d shows the seat area where profilometry scans were taken, along with the 2D wear patterns after 100 and 500 hours of test engine exposure. Figures 3a and b and Figures 4a-d show the same results for a representative TiAl valve (TiAl-5).

In addition to wear scar depth, a quantity that allows direct comparison of worn contact region is the surface roughness, or R_A. Table 3 illustrates the surface roughness of each Si_3N_4 and TiAl valve prior to engine aging and after the first 100 and 500 hours. Measurements were not available for the valve seat and TiAl valve guide after 500 hours.

Table 3. Surface roughness measurement of valves at 0 h and 100 h

	Valve ID #	Valve Location	Time (hrs)	Ra (Valve Guide)		Ra (Valve Seat)
Si3N4 Intake	Si3N4I-20	I2-SI3N4	0	0.067		0.152
			100	0.095		0.226
			500	0.058		NA
	Si3N4I-21	I4-SI3N4	0	0.061		0.15
			100	0.079		0.779
			500	0.05		NA
	Si3N4I-25	I6-SI3N4	0	0.069		0.143
			100	0.069		0.199
			500	0.046		NA
	Si3N4I-28	I8-SI3N4	0	0.063		0.178
			100	0.093		0.435
			500	0.057		NA
	Si3N4I-33	I10-SI3N4	0	0.067		0.174
			100	0.089		0.185
			500	0.059		NA
	Si3N4I-41	I12-SI3N4	0	0.069		0.174
			100	0.096		0.394
			500	0.053		NA
Si3N4 Exhaust	Si3N4E-11	E1-SI3N4	0	0.063		0.232
			100	0.059		0.436
			500	0.072		NA
	Si3N4E-17	E3-SI3N4	0	0.06		0.211
			100	0.027		0.888
			500	0.035		NA
	Si3N4E-9	E5-SI3N4	0	0.063		0.222
			100	0.037		0.382
			500	0.048		NA
	Si3N4E-32	E7-SI3N4	0	0.066		0.206
			100	0.034		0.389
			500	0.048		NA
				Ti	TiAl	
TiAl Exhaust	TiAl-5	E9-TiAl	0	0.121	0.071	0.187
			100	0.239	0.316	0.970
			500	0.178	NA	NA
	TiAl-6	E11-TiAl	0	0.102	0.063	0.221
			100	0.316	1.054	1.157
			500	0.181	NA	NA
	TiAl-7	E13-TiAl	0	0.121	0.054	0.211
			100	0.269	0.661	0.762
			500	0.119	NA	NA
	TiAl-8	E15-TiAl	0	0.12	0.052	0.226
			100	0.318	1.097	1.143
			500	0.165	NA	NA

Several preliminary conclusions may be drawn from these micrographs, profilometry scans and surface roughness measurements.

- **Valve/seat wear:** A 2x increase in valve/seat surface roughness after 100 hours for Si3N4E-32 is evidence of break-in scuffing wear on the Si_3N_4 valve. Figure 2b shows a relatively constant wear scar depth of ~2 m. The scar depth continues to increase to ~8 m after 500 hours (Figure 2c). However, the 5x increase in valve/seat surface roughness for TiAl-5 is an indication that the wear has exceeded standard break-in wear. This is confirmed by Figure 4b, which shows the valve/seat wear scar depth is ~15 m, a significant wear groove for only 100 engine hours. However, the wear seems to have reached a steady state, as the scar depth is only ~16 m after 500 hours (Figure 4c). Further conclusions will be determined on the wear resistance of TiAl and Si3N4 valves after the completion of the 1000 hours of engine exposure
- **Valve/guide wear:** The surface roughness data suggests that minor scuffing wear moderately increases the R_A of the Si_3N_4 intake valves after 100 hours. The R_A decreases after 500 hours due to polishing wear mode, which is enabled by higher stem temperatures at longer exposure times. This mechanism is seen initially in the Si_3N_4 exhaust valves because the exhaust temperatures are already at elevated temperatures after 100 hours. The R_A continues to increase after 500 hours of exposure. The TiAl valves exhibit inferior wear performance than the Si_3N_4 valves in the valve/guide region. However, the 2x-3x R_A increase in the Ti-6-4 segment of the stem indicates that the thermal oxidation heat treatment was more effective on Ti-6-4 material than on TiAl, which showed a 3x-10x R_A increase. Although results are unavailable, this trend can be expected to continue for the 500- and 1000-hour tests.
- **Valve integrity:** Although the wear mechanisms and rates must be better understood before Si_3N_4 and TiAl can be successfully implemented into production, the fact that these valves have survived 500 hours of service is an indication that these valves may be capable of withstanding a heavy-duty engine environment.

Valve Inspection – Laser Scatter NDE

At the end of the first 100- and 500-hour test phases the valves were scanned with the laser-based NDE instrument outlined in the project titled "NDE of Diesel Engine Components." Figures 5 and 6 show the NDE scans for exhaust valves Si3N4E-32 and TiAl-5 (the same valves in Figures 1 and 3). The region of interest is this valve seat band because this is the location of highest accumulated damage. A minor amount of wear was observed between 100 and 500 hours on the Si_3N_4 seat, while a significant amount of wear was observed on the TiAl seat for the same exposure time. The smooth continuous surfaces seen on the Si_3N_4 seats indicate that no or minor wear occurred. The defined light and dark ridges on the TiAl seats indicate that more significant, uneven wear occurred.

Next Steps

Since Phase #2 analysis has been completed, the next step is to complete Phase #3. About 2/3 of the valves will be re-installed in the engine, while the last 1/3 will be reserved for destructive testing. Also, due to the previously mentioned knocking phenomenon, the Si_3N_4 valves that previously in Cylinder 1 will be inserted into Cylinder 6. Production steel valves will be inserted into Cylinder 6. All of the production valves from Phase #2 will be replaced with new valves, since they were exposed to engine time not associated with this study. After the engine is run for another 500 hours, all valves will be removed, inspected and prepared for destructive testing. By performing fast fracture tests on valves that have accumulated 0, 500, 1000 hours of engine time, the effect of engine

aging on the materials' retained strength will be examined. Along with combustion dynamics and fuel consumption measurements, this data will enable the team to quantify the performance gains and durability of Si3N4 and TiAl valves in a heavy-duty engine environment.

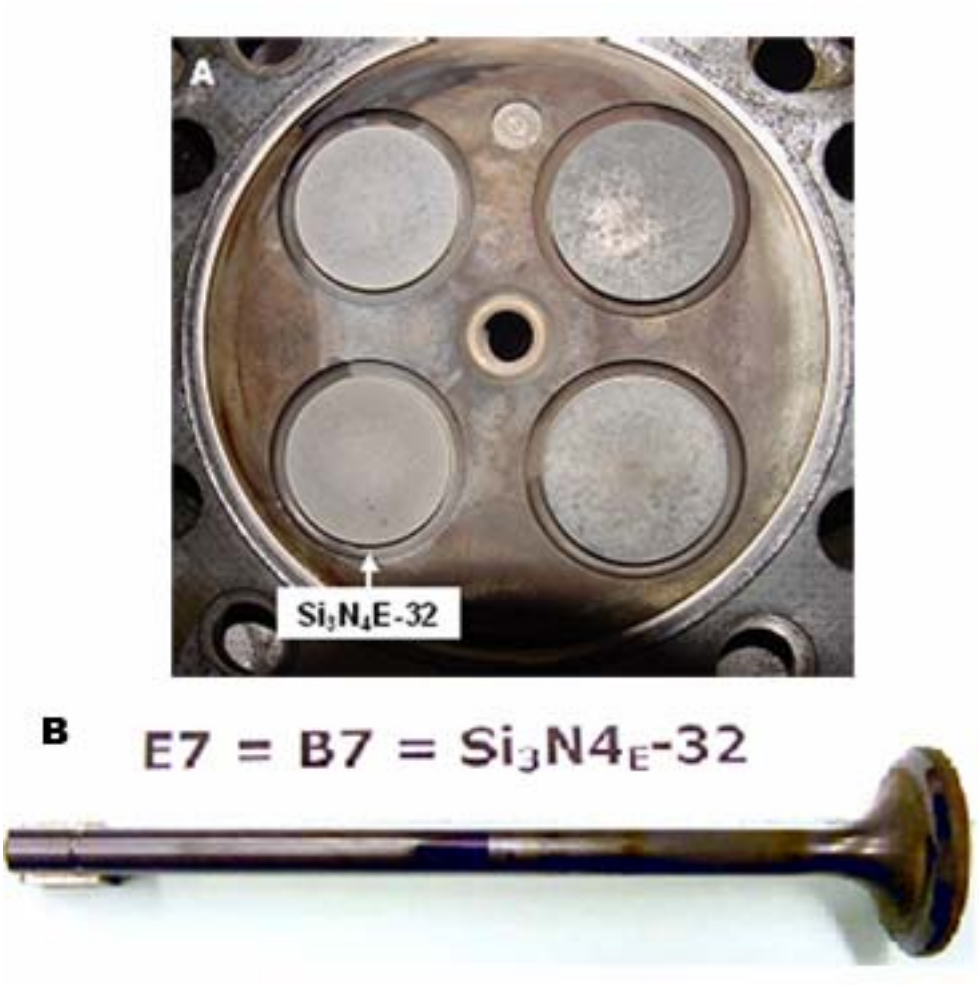

Figure 1. (A) An image of Cylinder 'B' immediately after the completion of the first 100-hour break-in phase.
(B) Valve Si3N4E-32, a representative Si_3N_4 exhaust valve after 500 hours.

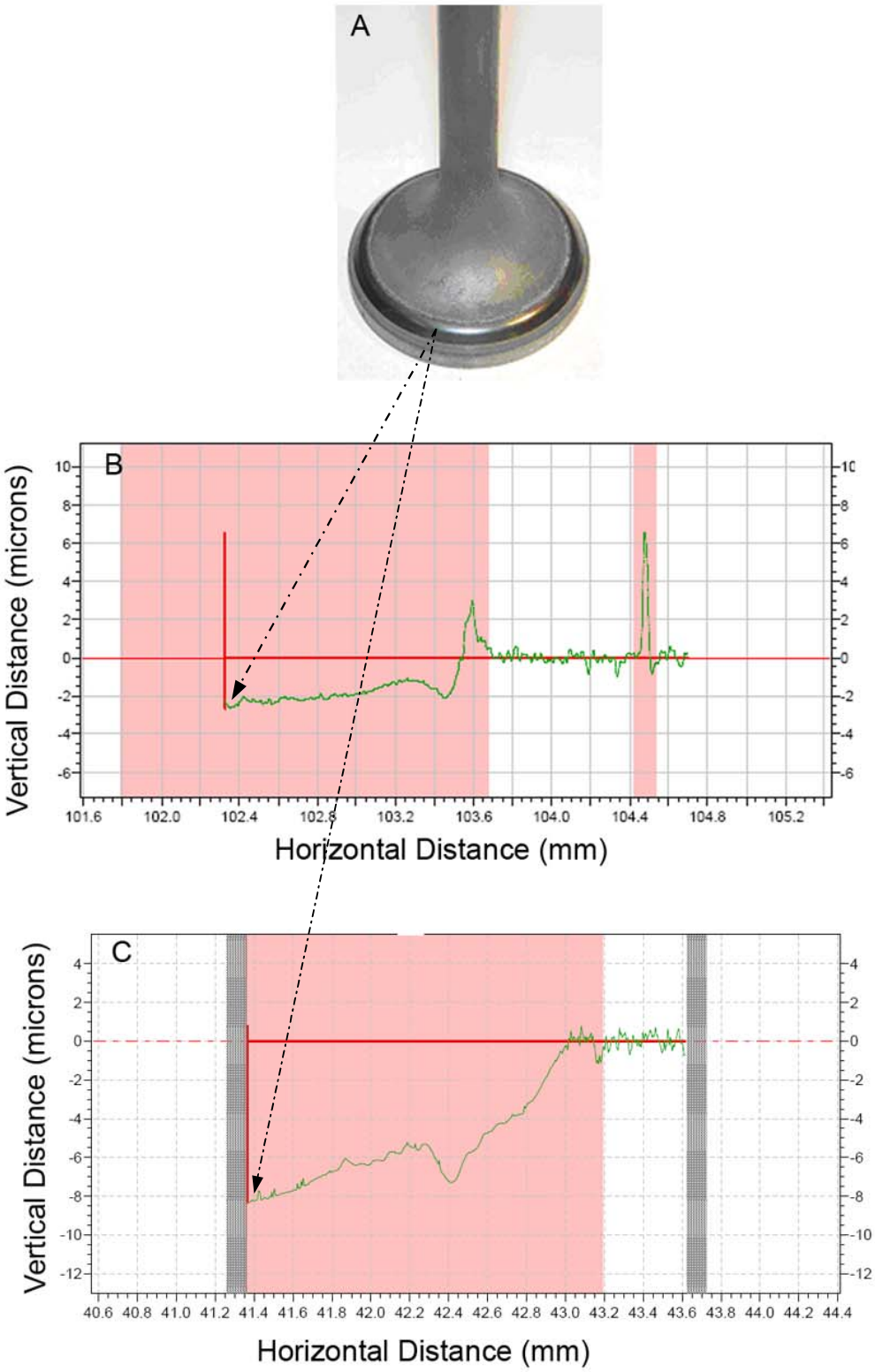

Figure 2. (A) Seat area where profilometry was taken from (B) 100-hour Si_3N_4 valve and (C) 500-hour Si_3N_4 valve.

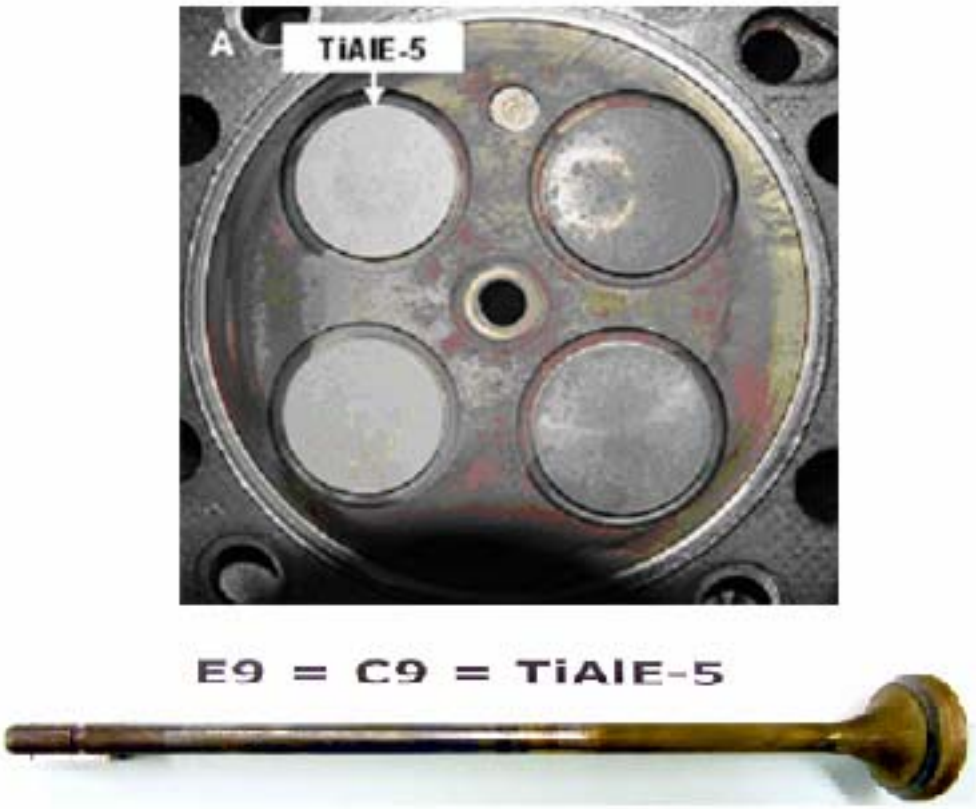

Figure 3. (A) An image of Cylinder 'B' immediately after the completion of the first 100-hour break-in phase.
(B) ValveTiAlE-5, a representative TiAl exhaust valve after 500 hours.

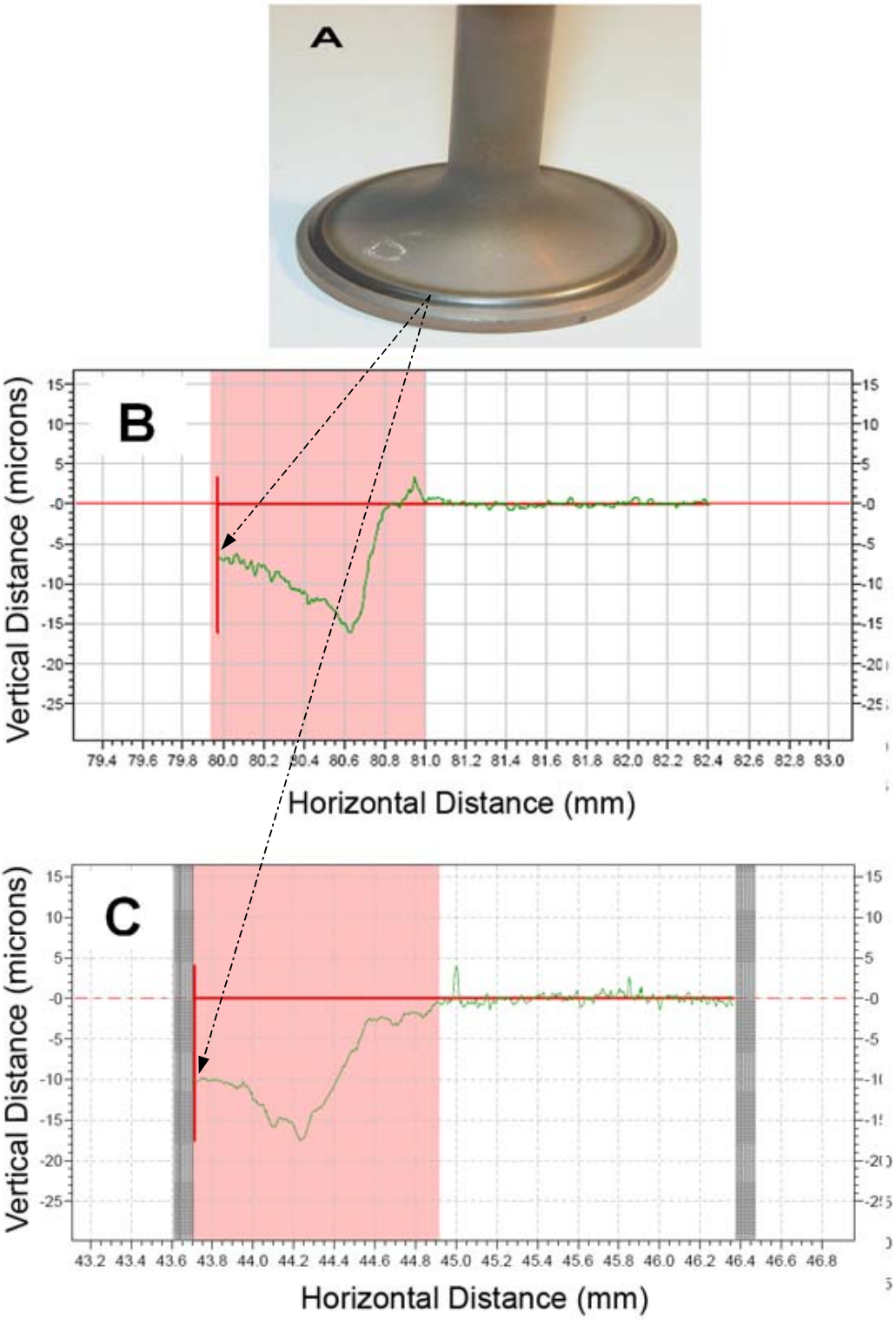

Figure 4. (A) Seat area where profilometry was taken from (B) 100-hour TiAl valve and (C) 500-hour TiAl valve.

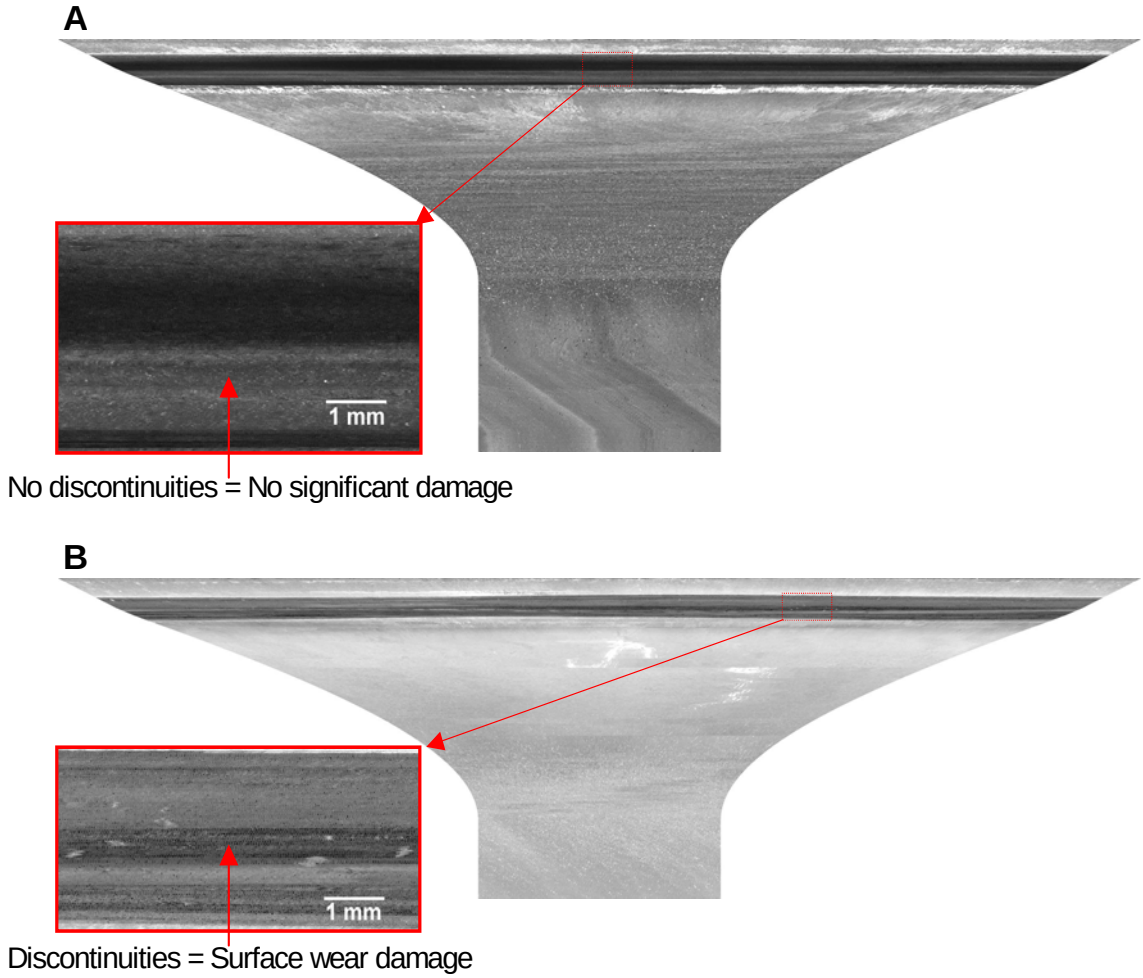

Figure 5. Laser-based NDE scans after 100 hours engine exposure time of (A) Si3N4E-32 and (B) TiAl-5 indicating that the Si_3N_4 valve has not sustained major wear damage, but the TiAl valve is showing signs of significant valve/seat wear.

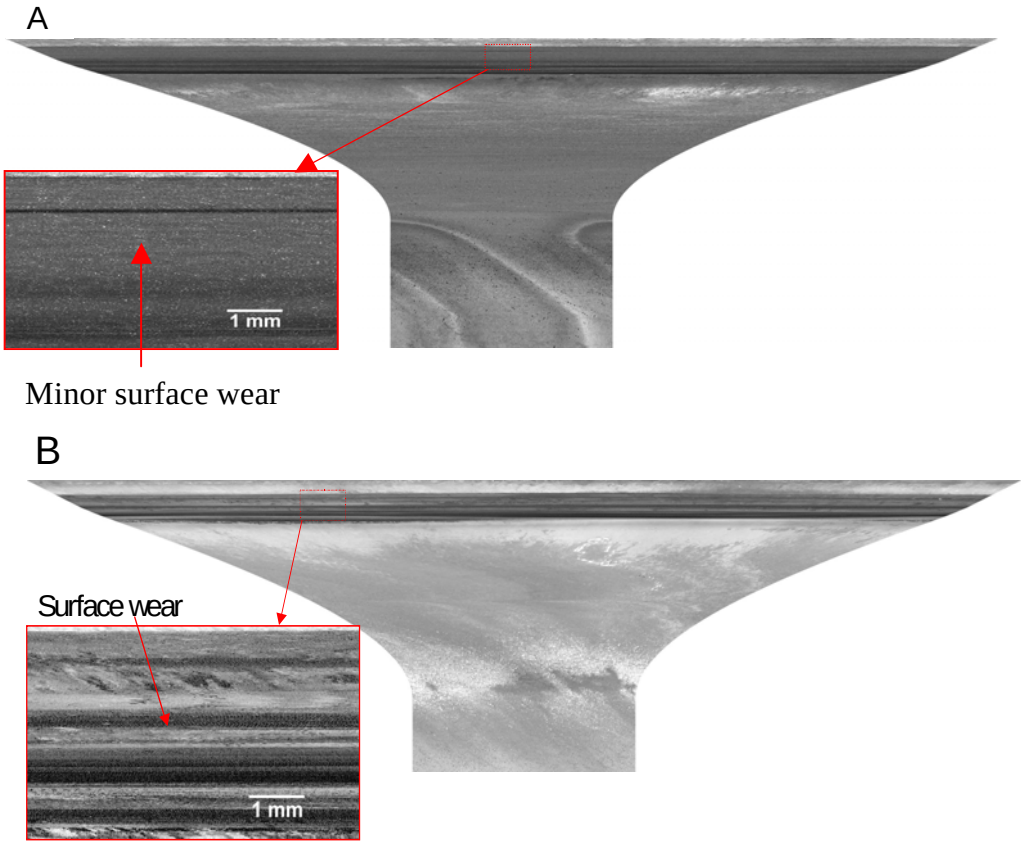

Figure 6. Laser-based NDE scans after 500 hours engine exposure time of (A) Si3N4E-32 and (B) TiAl-5 indicating that the Si_3N_4 valve has not sustained major wear damage, but the TiAl valve is showing signs of significant valve/seat wear.

NDE of Diesel Engine Components

J. G. Sun and N. Phillips*
Argonne National Laboratory
***Caterpillar, Inc.**

Objective/Scope

Emission reduction in diesel engines designated to burn fuels from several sources has lead to the need to assess ceramic valves to reduce corrosion and emission. The objective of this work is to evaluate several nondestructive evaluation (NDE) methods to detect defect/damage in structural ceramic valves for diesel engines. One primary NDE method to be addressed is elastic optical scattering. The end target is to demonstrate that NDE data can be correlated to material damage as well as used to predict material microstructural and mechanical properties. There are two tasks to be carried out: (1) Characterize subsurface defects and machining damage in flexure-bar specimens of NT551 and SN235 silicon nitrides (Si_3N_4) to be used as valve materials. Laser-scattering studies will be conducted at various wavelengths using a He-Ne laser and a tunable-wavelength solid-state laser to optimize detection sensitivity. NDE studies will be coupled with examination of surface/subsurface microstructure and fracture surface to determine defect/damage depth and fracture origin. NDE data will also be correlated with mechanical properties. (2) Assess and evaluate surface and subsurface damage in Si_3N_4 and TiAl valves to be tested in a bench rig and in an engine. All valves will be examined at ANL prior to test, during periodic scheduled shut downs, and at the end of the planned test runs.

Technical Highlights

Work during this period (October-December 2006) focused on acquisition and analysis of laser-scattering NDE data for 14 silicon-nitride (Si_3N_4) and titanium-aluminide (TiAl) valves that were tested in a Caterpillar natural-gas G3406 generator set for 500 hours at NTRC in ORNL.

1. Laser-Scatter NDE Evaluation of Engine-Tested Valves

During this period we acquired and analyzed laser-scattering NDE data for 10 Si_3N_4 and 4 TiAl valves that were run successfully for a total of 500 hours in a Caterpillar natural-gas G3406 generator set at the National Transportation Research Center (NTRC). In the 10 Si_3N_4 valves, 6 are intake valves (identified by I) and 4 are exhaust valves (identified by E); while all TiAl valves are exhaust valves. Figure 1 shows a photograph of these valves, including two standard steel valves I14 and I16. For these valves, the combustion coating deposited on the valve surface during the engine test has been cleaned before the NDE examination. The impact area is not entirely within the conical contact surface; it lies around the edge between the contact surface and the fillet surface, as illustrated in Fig. 2.

Fig. 1. Photograph of 500-hr engine-tested Si_3N_4 and TiAl valves.

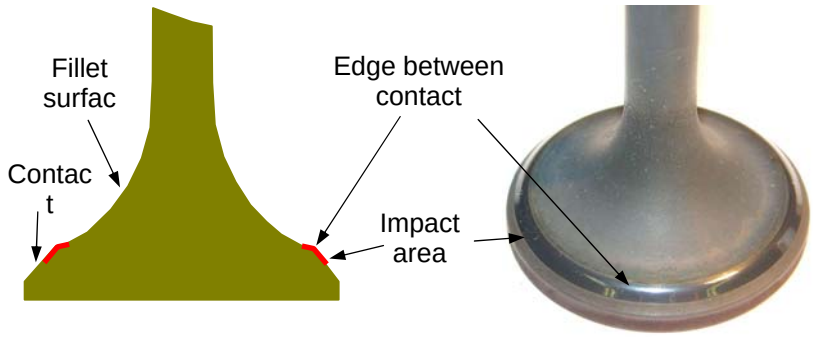

Fig. 2. Location of impact area on valve surface that was impacted with the seat insert.

NDE results representing typical valves of Si_3N_4 intake, Si_3N_4 exhaust, and TiAl exhaust are presented and discussed below. Laser-scatter image of the Si_3N_4 intake valve I2 after the 500-hr engine test is shown in Fig. 3. The scatter intensity in the impact area is slightly lower than that in the fillet and stem surface. Because subsurface damage always exhibits higher laser-scatter intensity, low scatter intensity in the impact surface is an indication of surface contamination. Within the impact area, shown in the enlarged NDE image in Fig. 3, no apparent subsurface damage was detected. The stripe pattern in the stem surface is due to the surface coloration variation.

Figure 4 shows the laser-scatter image of the Si_3N_4 exhaust valve E1 after the 500-hr engine test. Within the impact area, shown in the enlarged NDE image, many horizontal narrow bands of lower scatter intensity are detected. In addition, three wider bands of lower intensity are also observed, which were present in the NDE data from the 100-hr engine test (see Fig. 4 in our April-June 2006 report). Because a lower laser-scatter intensity does not indicate subsurface damage, the strong and complex NDE indications detected within the impact area should represent severe surface wear, not subsurface damage such as cracks or spalls.

Figure 5 shows the laser-scatter image of the valve-head surface of TiAl exhaust valve E9 after the 500-hr engine test. The scatter intensity in this image is scaled logarithmically in order to suppress the strong scatter from the coating on the fillet and stem surfaces. Two types of damage indications were observed from the NDE data. First, the impact region exhibits

considerable wear damage represented by distributed bands of high and low scatter intensities over the entire impact region. Second, several low scatter-intensity spots with sizes up to ~0.5 mm were detected within the impact region (see enlarged image in Fig. 5). Low scatter intensity from TiAl surface is usually an indication of significantly roughened surface. These results indicate that the impact damage in TiAl valves appears to be progressing at a faster rate than those observed in the Si_3N_4 valves. For the TiAl valve E11, which was installed in the same cylinder as E9, its NDE result is similar to E9. However, the NDE data for TiAl valves E13 and E15 which were installed together in another cylinder showed less prominent NDE indications, suggesting less damage as compared with that experienced by E9 and E11.

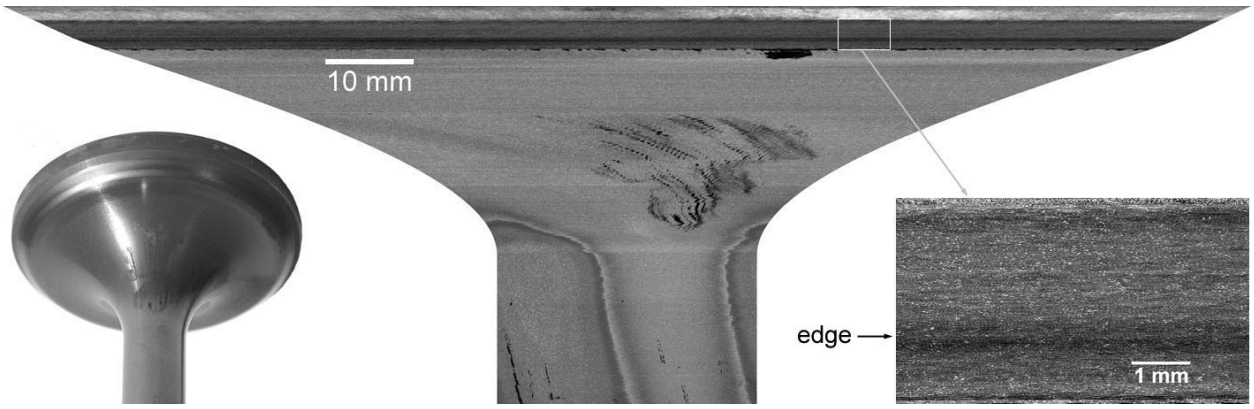

Fig. 3. Laser-scatter scan image of Si_3N_4 intake valve I2 after 500-hr engine test.

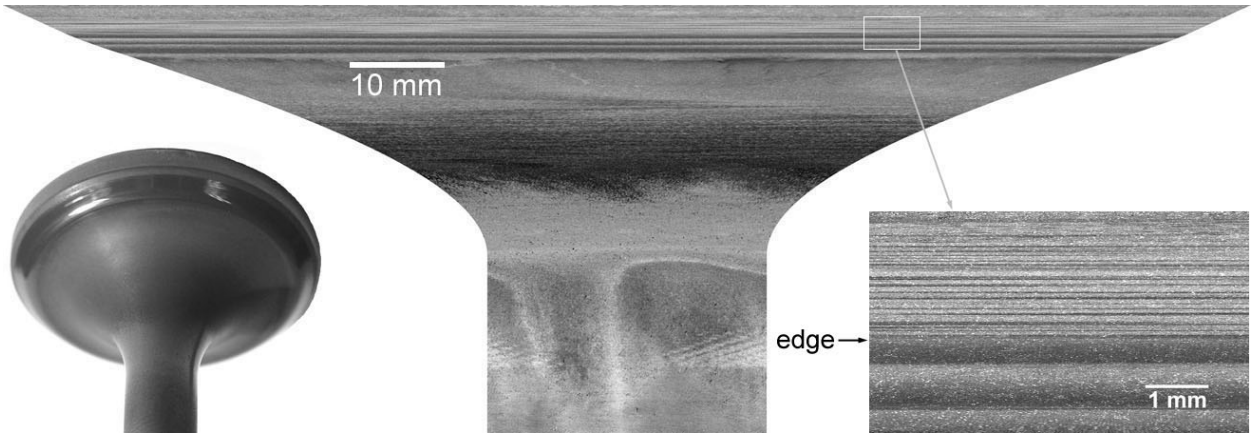

Fig. 4. Laser-scatter scan image of Si_3N_4 exhaust valve E1 after 500-hr engine test.

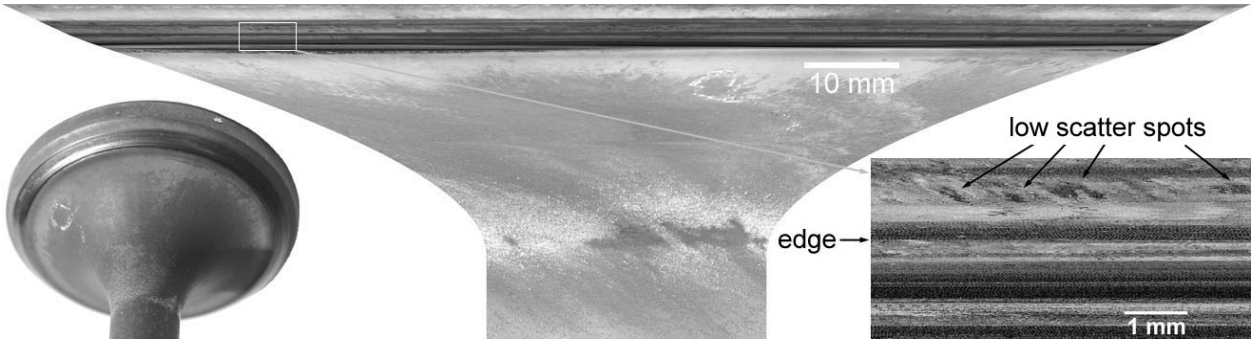

Fig. 5. Laser-scatter scan image of TiAl exhaust valve E9 after 500-hr engine test.

Figure 6 shows photomicrographs of impact surfaces of the Si_3N_4 intake valve I2, Si_3N_4 exhaust valve E1, and TiAl exhaust valve E9 after the 500-hr engine test. For intake valve I2, the machining surface mark has been worn off. The worn surface appears to be rough, making it susceptible for surface contamination as indicated from the NDE data (see Fig. 3). For exhaust valve E1, the impact surface displays considerable wear damage represented by narrow ridges and grooves that were detected in the NDE data (Fig. 4). It is unclear how these ridges/grooves were generated. For TiAl exhaust valve E9, however, several small "indents" and an apparent large (~0.5 mm) "pit" (from a spalled chip?) are observed. The pit surface appears rougher, which accounts for the lower scattering intensity from the spots detected in the NDE data (in Fig. 5). In addition, several wear grooves are observed in the impact surface of the TiAl valve. In general, the micrographic observations of these valves are consistent with those detected by the laser scatter NDE.

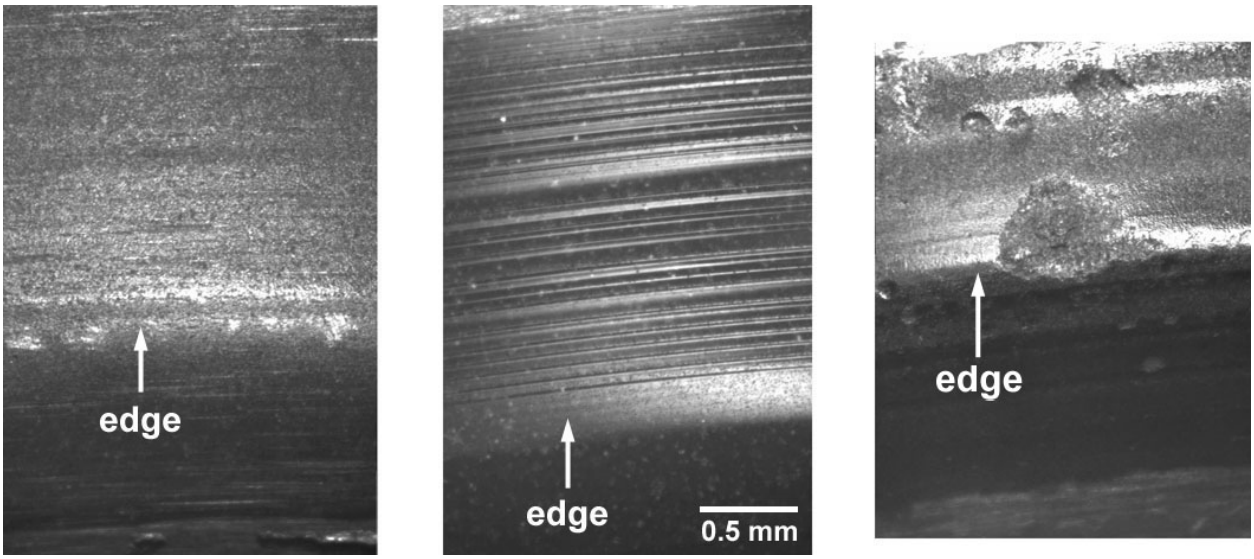

Si_3N_4 intake valve I2 Si_3N_4 exhaust valve E1 TiAl exhaust valve E9

Fig. 6. Photomicrographs of impact surfaces of Si_3N_4 and TiAl valves after 500-hr engine test.

The 14 Si_3N_4 and TiAl valves have been reinstalled in the natural gas G3406 generator set at the NTRC for the third and last phase of 500-hr testing. NDE inspection of these valves will be conducted after this phase is completed and results will be presented in the next period.

Status of Milestones

Current ANL milestones are on schedule.

Communications/Visits/Travel

J. G. Sun plans to present a paper at the 31st Int. Cocoa Beach Conf. & Exposition on Advanced Ceramics and Composites to be held January 21-26, 2007 in Daytona Beach, FL.

Problems Encountered

None this period.

Publications

None this period.

Life Prediction of Diesel Engine Components

H. T. Lin, T. P. Kirkland, Hong Wang, A. A. Wereszczak
Oak Ridge National Laboratory

Nate Phillips and Nan Yang
Caterpillar Inc.

Objective/Scope

The valid prediction of mechanical reliability and service life is a prerequisite for the successful implementation of structural ceramics and advanced intermetallic alloys as internal combustion engine components. There are three primary goals of this research project which contribute toward that implementation: the generation of mechanical engineering data from ambient to high temperatures of candidate structural ceramics and intermetallic alloys; the microstructural characterization of failure phenomena in these ceramics and alloys and components fabricated from them; and the application and verification of probabilistic life prediction methods using diesel engine components as test cases. For all three stages, results are provided to both the material suppliers and component end-users.

The systematic study of candidate structural ceramics (primarily silicon nitride) for internal combustion engine components is undertaken as a function of temperature (< 1200°C), environment, time, and machining conditions. Properties such as strength and fatigue will be characterized via flexure and rotary bend testing.

The second goal of the program is to characterize the evolution and role of damage mechanisms, and changes in microstructure linked to the ceramic's mechanical performance, at representative engine component service conditions. These will be examined using several analytical techniques including optical and scanning electron microscopy. Specifically, several microstructural aspects of failure will be characterized:

(1) strength-limiting flaw-type identification;
(2) edge, surface, and volume effects on strength and fatigue size-scaling
(3) changes in failure mechanism as a function of temperature;
(4) the nature of slow crack growth; and
(5) what role residual stresses may have in these processes.

Lastly, numerical probabilistic models (i.e., life prediction codes) will be used in conjunction with the generated strength and fatigue data to predict the failure probability and reliability of complex-shaped components subjected to mechanical loading, such as a silicon nitride diesel engine valve. The predicted results will then be compared to actual component performance measured experimentally or from field service data. As a consequence of these efforts, the data generated in this program will not only provide a critically needed base for component utilization in internal combustion engines, but will also facilitate the maturation of candidate ceramic materials and a design algorithm for ceramic components subjected to mechanical loading in general.

Technical Highlights

Silicon nitride and TiAl exhaust valves

During this reporting period the surface roughness of 400h-tested reference steel valves currently used in the commercial engine has been characterized. The measurement of surface roughness was carried out using a Taylor-Hobson surface profiling system (Model # Form Talysurf 120). Note that three sections; i.e., upper valve guide, lower valve guide, and valve seat insert contact region, were evaluated, and average values of three scans at each section were taken at 0, 120, and 240°, respectively. The surface roughness results of valve guide region showed that the reference steel valves exhibited Ra values that were 3-5 times greater than those obtained for both silicon nitride and TiAl valves. Also, the transition curvature region of reference steel valves showed substantial oil deposit resulting in an increased roughness, possibly resulting from the leakage of lubricant into the valve train. On the other hand, selected 500h-tested valves, which were fabricated from silicon nitride and TiAl, were machined for retained strength characterization after NDE evaluation at ANL. The objective of this destructive study was to evaluate the effect of the surface roughness introduced after 500h engine test on the mechanical reliability and performance. The half-cylindrical bend bars have been machined from the stem section and would be tested using the four-point flexure approach. Also, the valve-head section would be tested via a custom design fixture, as shown in Fig. 1, to see how the engine environment would alter the mechanical strength in the curvature transition region, which was subjected to the highest stress level during engine testing, after 500h exposure. Note that similar specimens machined from as-received valves would be tested for comparison. The mechanical strength results would be reported and compared in the next quarterly report. On the other hand, the preparation of fixtures and valves to be used for the next 500h engine test to achieve 1000h engine test data in total is now in progress.

TiAl intermetallic alloys

Studies of long-term creep behavior in air of TiAl alloys manufactured by Daido and Howmet were continued during this reporting period. Two types of TiAl cylindrical creep specimens different in final densification process (i.e., one is HIP and the other one is Non-HIP) manufactured by Daido, Tokyo, Japan were received from end user. Also, TiAl tensile specimens manufactured by Howmet, Michigan, USA were also received for evaluation. The test conditions specified are relevant to the temperature and stress profile encountered by TiAl turbo wheel under the application environments based on the FEA modeling. The database generated will then be used for verification of probabilistic life prediction of turbo wheel under engine operation conditions by the end users, and also could provide feedback to material suppliers for process modification to further improve mechanical properties. Preliminary tensile creep results of Daido TiAl alloy showed that there was a minor effect of processing (HIP vs. non-HIP) method on the high temperature creep behavior at 650°C. However, at temperatures ≥ 700°C the non-HIP TiAl specimens exhibited 10-times lower creep than that obtained for HIP TiAl specimen, as shown in Fig. 2. Also, the creep exponents (n) obtained from the slope of creep rate vs. applied stress curves showed the n valve obtained at 650°C is ~ 2.4 and it then transitioned to a much higher n valve of 13.4 at 750°C, indicating a change in creep controlling mechanism. On the other hand, the limited creep data indicated that the Daido HIP TiAl would exhibit lower creep rates as compared with those obtained for Howmet TiAl under similar test conditions. Nonetheless, more creep tests under various test temperatures and applied stress

levels would be carried out to understand the effect of microstructure on the creep response and also the creep controlling mechanism as a function of temperature and stress level. Detailed analysis of microstructure (grain size and phase content) of these three TiAl alloys would be performed as well.

Status of Milestones

Milestone: "Complete mechanical testing and analysis of prototype silicon nitride and TiAl valves after natural gas engine field test." On schedule.

Communications / Visitors / Travel

Communication with Nate Phillips at Caterpillar, and Norberto Domingo and Michael Kass at NTRC on the updated status of the preparation works for the next phase 500h engine test for Si_3N_4 and TiAl exhaust valves.

Communication with Nate Phillips at Caterpillar on the mechanical testing on the Ceradyne SN147 silicon nitride cylindrical rods after machined via various machining parameters.

Communications with Nan Yang at Caterpillar on the update of tensile creep tests for TiAl materials, and also discussions of the mechanical testing plans for FY2007.

Problems Encountered

None.

Publications

H. T. Lin, T. P. Kirkland, A. A. Wereszczak, and M. J. Andrews, "Strength Retention of Silicon Nitride After Long-term Oil Immersion Exposure," *J. Mater. Sci.* 41, 8313-8319 (2006)

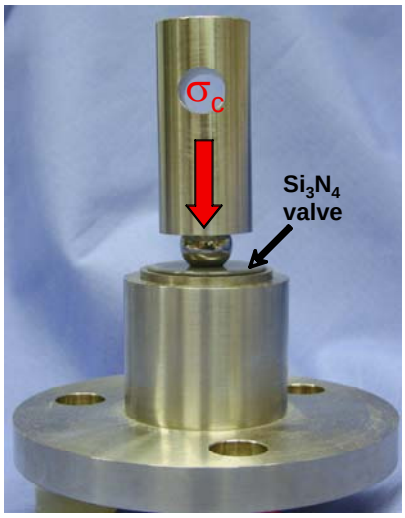

Figure 1. Photo of silicon nitride exhaust valve mechanical testing fixture. The test was carried out via a Universal Instron machine.

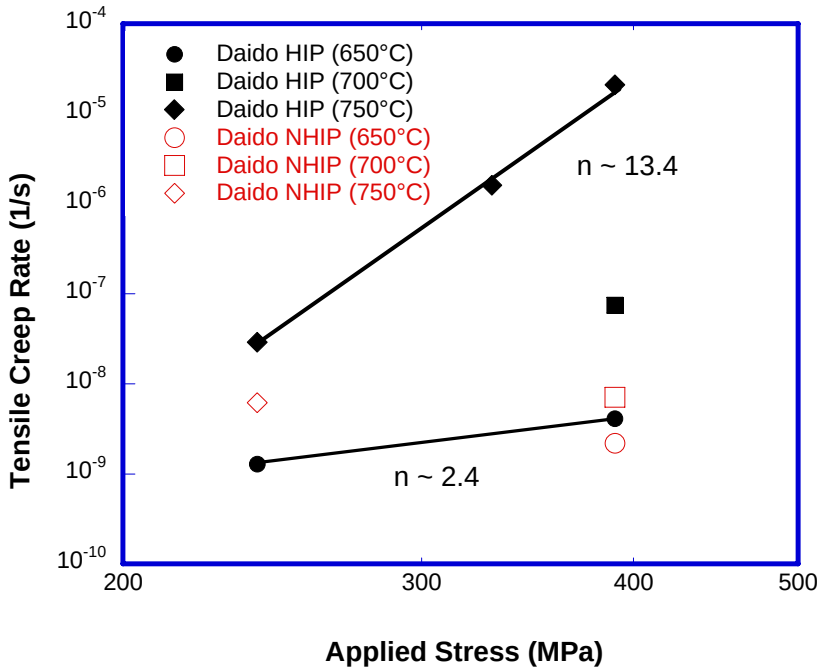

Figure 2. Creep rate versus applied stress of Daido TiAl with HIP and Non-HIP condition.

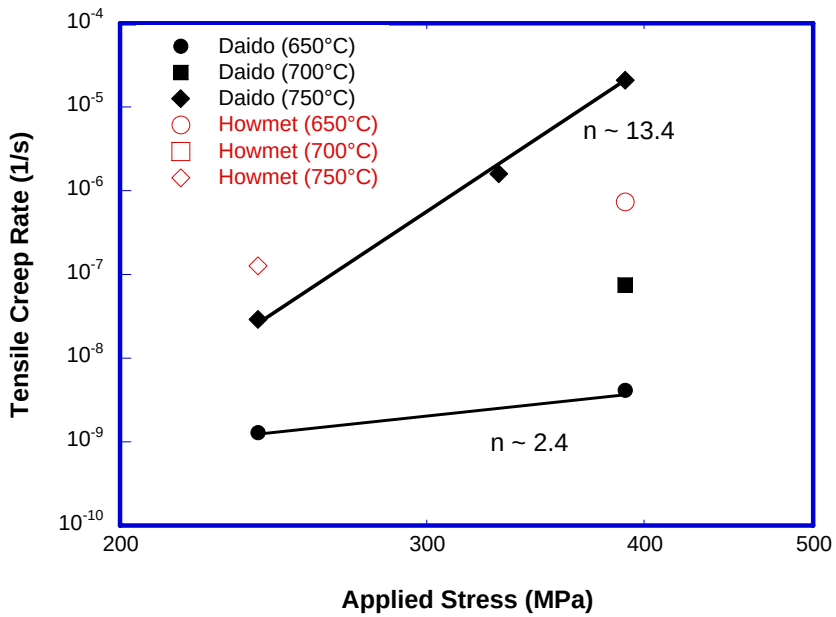

Figure 3. Creep rate versus applied stress of Daido and Howmet TiAl..

Modeling of Thermoelectrics

A. A. Wereszczak and H. -T. Lin
Ceramic Science and Technology (CerSAT)
Oak Ridge National Laboratory

Objective/Scope

Potential next generation thermoelectric (TE) devices comprised of p- and n-type oxide ceramics enjoy strong interest for implementation in high temperature and oxidizing environments because their waste heat could be used to generate electricity. However, the intended TE function of these devices will only be enabled if the device is designed to overcome the thermomechanical limitations (i.e., brittleness) inherent to these oxides. A TE oxide with a combination of poor strength and low thermal conductivity can readily fail in the presence of a thermal gradient thereby preventing the exploitation of the desired thermoelectrical function.

This seemingly insurmountable problem can be overcome with the combined use of established probabilistic design methods developed for brittle structural components, good thermoelastic and thermomechanical databases of the candidate oxide material comprising the TE device, and iteratively applied design sensitivity analysis. This project executes this process by interrogating the reliability of prototypical TE devices (e.g., thin-film-based) and oxides.

There will be several outcomes from this work that will benefit TE oxide and device developers and end-users of these potentially high temperature TE devices: mechanical reliability of prototypical TE devices will be evaluated from a structural ceramic perspective and suggested redesigns will be identified, thermomechanical reliability of developmental TE oxides will be assessed, and minimum required thermomechanical properties of hypothetical TE oxides would be identified that produce desired reliability in a TE device. Additionally, innovative and cost-effective methods to process high temperature capable TEs will be a part of this project's research portfolio.

Technical Highlights

Finite element modeling analysis of TE devices and their constituents is a primary effort to this project. An example of preliminary modeling is shown in Fig. 1. Preparation for probabilistic design sensitivity (PDS) analysis and modeling occurred during the present reporting period. PDS analysis will be enabled using commercial FEA software (ANSYS). It will determine the sensitivity of the developed stresses (or probability of failure) in the TEs to the variability of the geometry, properties of the TE device material constituents, and the loading or service/ boundary/initial conditions. The outcome of this analysis will show which of the parameters would most influence TE device failure probability. For example, it could be found that simply changing the processing temperature (i.e., strain-free-temperature) could substantially reduce stress development in a TE device. A simple illustration of PDS analysis is shown in Fig. 2.

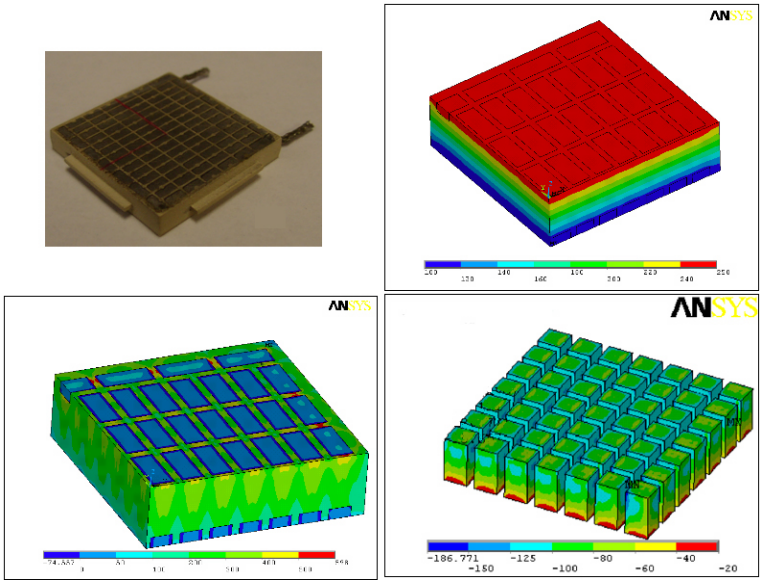

Figure 1. A whole TE device is shown in the upper left; however the other images are from one-quarter symmetry analysis. Shown here are some arbitrary finite element thermal and stress analyses of such a device that our team have performed.

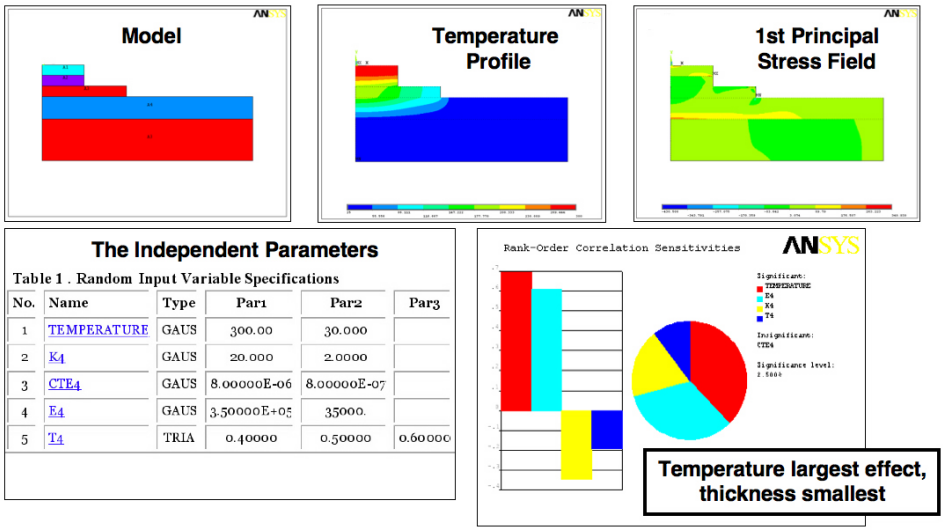

Figure 2. In this example of PDS analysis, it was asked "Which of the unknowns of temperature gradient or the alumina substrate's thermal conductivity or its coefficient of thermal expansion or its elastic modulus or its thickness has the greatest effect on the generated tensile stress within it?" Referring to the bottom right hand visual, temperature (red) and the alumina substrate's elastic modulus (teal) have the highest influence on stress in the alumina, followed by thermal conductivity (yellow) and thickness (blue). The coefficient of thermal expansion for alumina has negligible effect on stress within the variation set in this example.

Status of FY 2007 Milestones

Perform probability design sensitivity analysis on a TE device and rank those material properties or dimensions whose control would have the largest effect on reliability. **(Sep07)** *On schedule.*

Communications/Visits/Travel

Norbert Elsner of Hi-Z Technologies, Inc. (San Diego, CA) met with A. A. Wereszczak to discuss needs for thermomechanical stress modeling and design optimization of thermoelectric modules, and the consideration of silicon nitride as a substrate candidate.

Publications

None.

References

None.

Powder Processing of Nanostructured Alloys Produced by Machining

S. Chandrasekar, K. P. Trumble, and W. D. Compton
College of Engineering
Purdue University

Objective/Scope

Work continued on low-temperature consolidation routes for ultrafine-grained alloy particulate produced by machining. This report focuses on the latest results in polymer bonding of Al-6061-T6 chip particulate.

Technical Highlights

Epoxy-bonded Al-6061-T6 machining chip particulate

The goal of this approach is to bond the machining chip particulate with a thin polymer bond layer, the epoxy cure at 100°C only slightly degrading the hardening imparted in chip formation. Two routes have been developed, (1) premixing the alloy powder and liquid epoxy and pressing in a closed die having sufficient clearance that the excess epoxy is squeezed out and (2) prepressing the alloy powder alone followed by isostatic pressure infiltration. Premixing the liquid epoxy seems to introduce bubbles that are not eliminated in pressing since the effective pressure on the liquid is only atmospheric pressure. Whereas, prepressing the powder results in the formation of closed pores, which are not penetrated by the liquid epoxy during high-pressure infiltration (210 MPa). Nevertheless, composites containing over 90 volume percent metal have been produced.

A previous report focused on the effects of particle shape and surface oxides. Equiaxed particles produced by modulation-assisted machining exhibited more uniform packing, although the metal volume fraction was comparable to that achieved with the high aspect ratio powders produced by milling. This report focuses on the effects of basic processing parameters, pressing pressure and epoxy viscosity, on composite microstructure, density and hardness.

Figure 1 shows optical micrographs of composites produced using two different epoxies ("thin" and "thick") and two different pressing pressures. The M-bond is a thin epoxy used for glue-on strain gages and TEM specimen preparation. Its low viscosity ($\eta \sim 1$ mPa·s) comes with the disadvantage of high cure shrinkage. Figure 1(a) and (b) show the effect of doubling the pressing pressure from 500 to 1000 MPa, whereas Fig. 1(c) shows the effect of using an epoxy of more conventional viscosity ($\eta \sim 600$ mPa·s) at a pressing pressure of 1000 MPa. The higher viscosity resulted in a thicker "glue" layer between the particles.

Density measurements combined with quantitative stereology allow the volume fractions of all three phases (alloy, epoxy, and porosity) to be determined. Since the density of all three constituents is known, a stereological measurement of the metal volume fraction by systematic point counting allows the volume fraction of porosity and epoxy to be distinguished. The results are shown in Table 1.

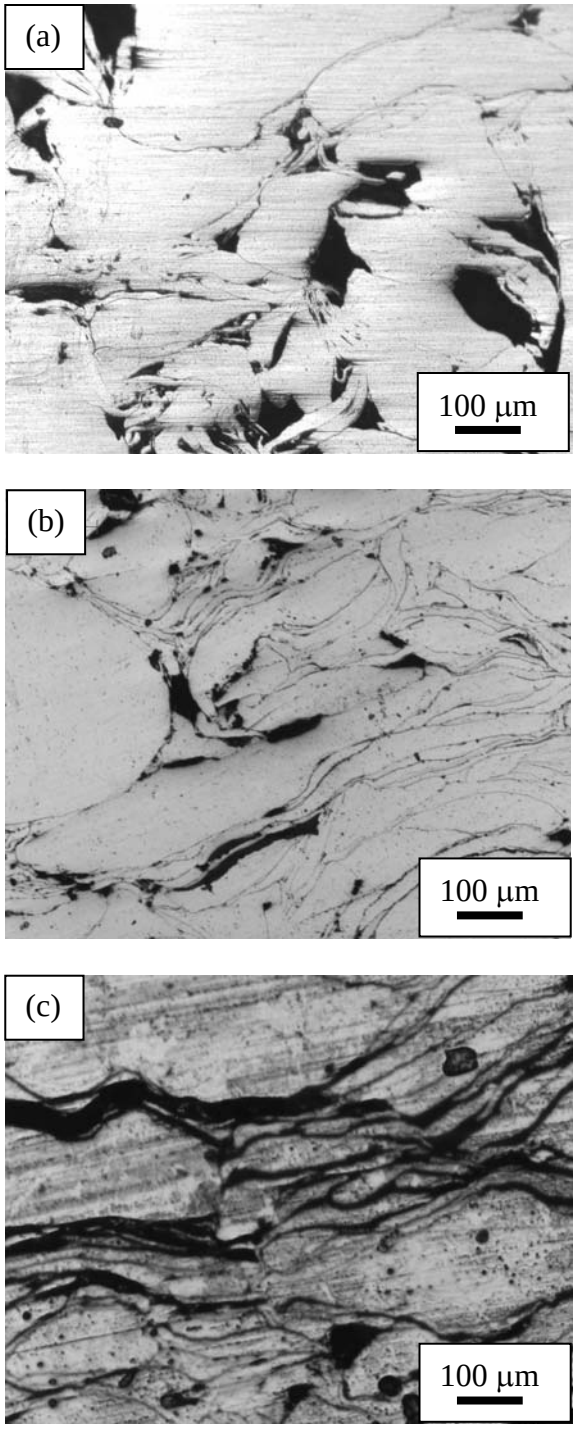

Figure 1 - Optical micrographs showing the effect of pressing pressure and epoxy viscosity on composite microstructure. Al-6061-T6 chip powder produced by milling and mixed with liquid epoxy: M-bond epoxy (η ~ 1 mPa·s) pressed at 500 MPa (a) and 1000 MPa (b), Epoxide epoxy (η ~ 600 mPa·s) pressed at 1000 MPa.

The primary effect pressing pressure increasing the alloy volume fraction is apparent. Since the density of the alloy is the highest of the three constituents (ρ_{alloy} = 2.70 g/cm^3, $\rho_{M\text{-}bond\ epoxy}$ = 1.04 g/cm^3, $\rho_{Epoxide\ epoxy}$ = 1.12 g/cm^3) and $V_{alloy} = 1 - (V_{epoxy} + V_{porosity})$, pushing the alloy particles closer together (squeezing out more epoxy) yields a higher density.

Table 1 - Composite processing conditions and resulting density, phase volume fractions and average hardness.

Epoxy Type	Pressing Pressure (MPa)	Density (g/cm^3)	V_{alloy}	V_{epoxy}	$V_{porosity}$	Hardness (kg/mm^2)
M-bond	500	2.22	0.81	0.04	0.15	108
M-bond	1000	2.39	0.88	0.02	0.10	116
Epoxide	1000	2.42	0.88	0.05	0.07	120

The metal volume fraction also has a primary effect on the composite hardness. These values are the average of 10 measurements using a 100-kg load. The starting chip hardness is about 150 kg/mm^2, whereas the starting alloy before machining (T6 condition) is about 107 kg/mm^2. These results indicate that a significant fraction of the hardening imparted by the machining is retained in this process. These results point out the need for a model to describe the composite hardness in terms of the constituent hardness values and composite microstructure. With such a model we hope to be able to determine the relative importance of alloy volume fraction and strength of the alloy-epoxy bond.

Problems Encountered

None

Status of Milestones

"Evaluate consolidation routes enabling bulk monolithic and composite materials to be produced from nanostructured machining chip particulate without significant coarsening." On schedule.

Publications

1) M. Ravi Shankar, R. Verma, B. C. Rao, S. Chandrasekar, W.D. Compton, A.H. King and K.P. Trumble, Severe Plastic Deformation of Difficult-To-Deform Materials at Near-Ambient Temperature, *Metallurgical and Materials Transactions*, in press.

2) S. Saminathan, M. R. Shankar, B. C. Rao, W.D. Compton, S. Chandrasekar, A. H. King, K. P. Trumble, A New Approach for Studying Microstructure Refinement by Large Strain Deformation in Metals and Alloys, *Journal of Materials Science*, in press.

Visitors

Prof. Terry McNelley, Naval Postgraduate School, Monterey, CA, November 2007.

Student Graduated

None